https://doi.org/10.5194/essd-2026-443
Preprint. Discussion started: 24 June 2026

Open Access Earth System Science Data Discussions

A gapless 0.05° hourly tropospheric NO_2 dataset (2019–2024) over key Asian hotspots reconstructed using physics-aware deep learning

Hongrui Gao[1], Qin He[1*], Kai Qin[1*], Jhoon Kim[2], Diego Loyola[3], Pravash Tiwari[1], Lingxiao Lu[1], Jason B. Cohen[1]

[1]School of Environment and Spatial Informatics, China University of Mining and Technology, Xuzhou, China

[2]Department of Atmospheric Sciences, Yonsei University, Seoul, South Korea

[3]German Aerospace Center (DLR), Remote Sensing Technology Institute (IMF), Oberpfaffenhofen, Germany

**Correspondence to:* heqin@cumt.edu.cn / qinkai@cumt.edu.cn

Abstract. High-frequency continuous monitoring of tropospheric nitrogen dioxide (NO_2) is crucial for assessing regional air quality and investigating photochemical dynamic evolution. Although new-generation geostationary orbit (GEO) satellites (e.g., GEMS) provide hourly observations, their spatial coverage is often severely compromised by cloud obstruction and inherent retrieval limitations. Furthermore, their short observation history hinders long-term, cross-regional environmental assessments. To address this, this study presents a gapless, 0.05° hourly tropospheric NO_2 vertical column density (VCD) dataset for representative hotspots in Asia spanning 2019 to 2024, reconstructed using a physics-aware deep learning framework. The framework integrates partial convolutions to handle irregularly missing satellite observations and proposes a Physics-aware Normalization (PhysNorm) module. PhysNorm dynamically modulates 0.05° high-resolution feature maps using 0.25° low-resolution physical features such as ERA5 meteorological fields and EAC4 chemical priors, thereby ensuring rigorous physical continuity while filling data gaps. Validation results show that the model performs exceptionally on the test set (R^2 = 0.889) and maintains high generalization stability in an independent validation on 2024 data, which was not used for training. Cross-validation against an independent polar-orbiting satellite (GOME-2C) confirms the reliability of the dataset in reconstructing pollution hotspots and its applicability to periods without GEMS observations (2019–2022). Using this reconstructed dataset, this study finely delineates the periodic diurnal characteristics of NO_2 in typical Asian regions and accurately captures the inter-annual concentration gradients driven by public health events and emission reduction policies over the past six years. This newly generated dataset provides an unprecedented spatiotemporally continuous record, overcoming the limitations of cloud cover and short observational histories, thereby facilitating long-term, high-resolution air quality assessments and epidemiological studies. This dataset is available at https://doi.org/10.5281/zenodo.20427767 (Gao et al., 2026).

https://doi.org/10.5194/essd-2026-443
Preprint. Discussion started: 24 June 2026

Open Access Earth System Science Data Discussions

1. Introduction

Nitrogen dioxide (NO_2), a critical tropospheric trace gas and the primary constituent of nitrogen oxides (NO_x = NO + NO_2), predominantly originates from anthropogenic fossil fuel combustion, biomass burning, and biogenic soil emissions (Beirle et al., 2011; Purchase et al., 2023; Chang et al., 2025). As a crucial precursor to tropospheric ozone (O_3) and secondary aerosols, NO_2 profoundly impacts regional and global air quality (Wang et al., 2021; Baruah et al., 2022). Furthermore, by participating in the hydroxyl radical (OH) cycle, NO_2 directly modulates the atmospheric oxidative capacity and the transformation rates of other pollutants (Monks et al., 2009). Elevated NO_2 concentrations pose significant threats to human health, causing damage to the respiratory system and increasing the risk of asthma and cardiovascular diseases (Burnett et al., 2004; Samoli et al., 2006; Kampa and Castanas, 2008). Because of its short lifetime (typically ranging from a few hours to a day), the spatial distribution of NO_2 exhibits pronounced spatial heterogeneity and temporal variability, making it a widely adopted indicator for assessing atmospheric environmental changes and evaluating the effectiveness of emission control policies (Lamsal et al., 2013a; Goldberg et al., 2019). Given these environmental and health implications, continuous and accurate monitoring of NO_2 through diverse technical approaches remains a core research imperative in the atmospheric and environmental sciences.

Traditional ground-based monitoring networks provide NO_2 observations with high temporal resolution and accuracy. However, they are unevenly distributed, and their spatial coverage remains inherently limited, rendering them inadequate for large-scale monitoring requirements (Wei et al., 2022; Ahmad et al., 2024; Gu et al., 2025). In contrast, satellite remote sensing, characterized by its extensive and continuous observational capabilities, has undergone substantial development over the past few decades, emerging as a mainstream approach for regional and global NO_2 monitoring (Safieddine et al., 2013; Liu et al., 2021c; Li and Wu, 2021). Since the Global Ozone Monitoring Experiment (GOME) first measured global NO_2 column densities in the 1990s (Burrows et al., 1999), a succession of sensors, including SCIAMACHY, OMI, and GOME-2 has been launched (Bovensmann et al., 1999; Levelt et al., 2006a, b; Callies et al., 2000). These instruments enabled the study of global distribution and long-term NO_2 trends (Richter et al., 2005; Boersma et al., 2011a; Russell et al., 2012; Duncan et al., 2016; Krotkov et al., 2016; Liu et al., 2021b; Chan et al., 2023). In October 2017, the TROPOspheric Monitoring Instrument (TROPOMI) was launched onboard the Sentinel-5 Precursor satellite (Veefkind et al., 2012a). TROPOMI improved the spatial resolution from the 13 × 24 km^2 offered by OMI to 3.5 × 5.5 km^2, while maintaining daily global coverage. However, LEO satellites are limited by their orbital characteristics and can only provide daily observations. This sampling frequency is insufficient to resolve the diurnal dynamics of NO_2 driven by morning and evening traffic peaks, industrial activity cycles, and photochemical processes. To address this, Geostationary Earth Orbit (GEO) satellites have been deployed to increase temporal resolution. In February 2020, the Geostationary Environment Monitoring Spectrometer (GEMS) onboard the GEO-KOMPSAT-2B (GK-2B) satellite became operational (Kim et al., 2020a), providing 6–10 hourly observations per day of air quality over East and Southeast Asia (Choi et al., 2024; He et al., 2024a). Together with the Tropospheric Emissions: Monitoring of Pollution (TEMPO launched on 7 April 2023) over North America and Copernicus Sentinel-4 over Europe (launched on 1 July 2025 onboard EUMETSAT's Meteosat Third Generation Sounder (MTG-S1)), GEMS forms part of the global geostationary constellation for monitoring air quality, promising near-continuous, high-frequency observations over the major emission regions (Ingmann et al., 2012; Zoogman et al., 2017).

Nevertheless, the ideal scenario of global hourly monitoring remains a distant prospect. First, regardless of whether considering the pioneering GEMS or the subsequent TEMPO and Sentinel-4, the available temporal record of these instruments is relatively short, constraining the application of high-temporal-resolution data to longer-term atmospheric environment studies, policy assessments, and health impact analyses. Second, data completeness is a major challenge. The daily frequency of valid observations varies due to seasonal changes in solar illumination and daylight duration. In addition, due to cloud contamination

https://doi.org/10.5194/essd-2026-443
Preprint. Discussion started: 24 June 2026

Open Access Earth System Science Data Discussions

and high aerosol loading, the number of valid pixels in retrieved products can be significantly reduced (Boersma et al., 2004; Belle and Liu, 2016; Lee et al., 2025), making spatiotemporal gap-filling an essential step to enhance data completeness and usability. These considerations motivate a compelling research topic: based on the existing LEO satellite data, combined with other auxiliary information, to construct a temporally extensible and spatially near-seamless hourly tropospheric NO_2 dataset in time. To address this question, a method based on TROPOMI data and a series of auxiliary data to simulate the observation capability of GEMS is proposed in this study. It attempts to extend the hourly data to the time periods when GEMS does not have observations, even before launch, so as to provide more complete data support for scientific research in Asia, and contribute experience for future multi-sensor collaboration.

There are already a considerable number of studies related to the construction of long-term, high-coverage remote sensing datasets. Early spatiotemporal gap-filling approaches for individual satellite sensors were rooted primarily in geostatistical principles, such as Kriging interpolation and its derivatives (Hengl et al., 2007; Zammit-Mangion et al., 2018; Chen et al., 2020). Data Interpolating Empirical Orthogonal Functions (DINEOF), which reconstructs missing information by extracting the dominant spatiotemporal modes of the dataset, has been applied not only in oceanography (Alvera-Azcárate et al., 2005), but also to atmospheric products (Jiang et al., 2022; Qin et al., 2024). Supported by auxiliary data, Land Use Regression (LUR) models and Geographically Weighted Regression (GWR) have been extensively utilized in urban-scale air quality assessments by establishing statistical relationships between pollutant concentrations and spatial variables such as land-use types and population density (Hoek et al., 2008; Beelen et al., 2013; Meng et al., 2015; Qin et al., 2017). However, these traditional methods exhibit limitations when addressing complex, multi-source, heterogeneous data fusion tasks. In recent years, machine learning algorithms have been widely adopted in the fusion and prediction of remote sensing data (Peng et al., 2024), including Random Forest (RF), Gradient Boosting Decision Trees (GBDT), and Light Gradient Boosting Machine (LightGBM) (He et al., 2020; Kang et al., 2021; Fu et al., 2023; Ma et al., 2023; Shao et al., 2023; Wang et al., 2023). Also, within the atmospheric remote sensing domain, deep learning has been successfully deployed across various tasks, including the improvement of satellite retrieval algorithms (Loyola, 2006; Xu et al., 2017; She et al., 2020; Rao et al., 2022; Fan et al., 2023; She et al., 2024; Wei et al., 2025), the reconstruction of data gaps caused by cloud cover and other factors(Yu and Liu, 2021; Li et al., 2023; He et al., 2024b; Qu et al., 2025; Zhang et al., 2025a; Wang, 2026), and the establishment of more accurate mapping relationships between satellite column observations and surface-level concentrations (Sun et al., 2019; Scheibenreif et al., 2022; Xing et al., 2024; Li et al., 2025; Handschuh et al., 2026). Despite these advances, existing deep learning models often struggle to effectively manage non-random missing patterns in satellite observations. Simplistic interpolation or masking strategies ignore the spatial continuity between valid observational pixels and their surrounding missing regions. Moreover, conventional deep learning architectures typically integrate meteorological variables or physical constraints through straightforward channel-level concatenation, lacking an in-depth characterization of the dynamic modulation between atmospheric physical processes and pollutant distributions.

To address this, this study proposes PhysNorm-Net, a physics-aware network to reconstruct a gapless 0.05° hourly tropospheric NO_2 dataset. This architecture is designed to fuse multi-source heterogeneous satellite data with physical and meteorological priors, achieving high-precision, spatiotemporally continuous tropospheric NO_2 vertical column density (VCD) reconstruction. The value and major contributions of this dataset are summarized as follows: 1) High spatiotemporal completeness and resolution: It provides the first seamless hourly NO_2 records at 0.05° resolution covering both pre- and post-GEMS periods, effectively mitigating data gaps caused by cloud contamination and observation limitations. 2) Physical consistency: Instead of simple statistical interpolation, the dataset generation is strictly constrained by meteorological and chemical priors, ensuring that the reconstructed concentration fields adhere to atmospheric physical continuity. Independent validation confirms its robust inter-annual stability. 3) Enhanced utility for long-term environmental analysis: The dataset enables fine-grained delineation of

https://doi.org/10.5194/essd-2026-443
Preprint. Discussion started: 24 June 2026

previously obscured periodic diurnal characteristics and accurately captures inter-annual concentration gradients driven by socioeconomic changes over the past six years.

2. Study area and data

2.1 Study area

This study selects four typical regions encompassing diverse climatic zones, emission characteristics, and topographical complexities, as detailed in Table 1.

Table 1: Four representative study regions and their geographical extents selected in this study.

Region	Abbreviation	Latitude	Longitude
North China Plain	NP	34–44°N	112–122°E
Sichuan Basin and surroundings	CC	26–36°N	100–110°E
Korea and Japan	KJ	32–42°N	126–136°E
Northern India	NI	20–30°N	75–85°E

The North China Plain (NP) is one of China's largest plains, characterized by intensive heavy industrial and traffic emissions. The Sichuan Basin and its surrounding areas, encompassing major urban centers such as Chengdu and Chongqing (CC), are defined by an enclosed topographic configuration that severely restricts atmospheric ventilation and promotes pollutant accumulation, thereby producing a topographically driven atmospheric environment fundamentally distinct from that of the other study regions. The Korea and Japan (KJ) region spans the Korean Peninsula and the Japanese archipelago, where NO_2 distributions are significantly influenced by transboundary transport and maritime climatic conditions. Northern India (NI), situated in the Indo-Gangetic Plain, experiences frequent winter haze episodes and agricultural biomass burning. Given the high spatial heterogeneity of NO_2 distributions, the selection of these four representative regions maximizes information density and gradient diversity within the training sample.

2.2 GEMS tropospheric NO_2 data

The Geostationary Environment Monitoring Spectrometer (GEMS), an ultraviolet-visible (UV-Vis) imaging spectrometer onboard the GEO-KOMPSAT-2B (GK-2B) satellite, was launched in February 2020 and became operationally active in November 2022 following in-orbit testing. GEMS provides spectral measurements from 300 to 500 nm with a spectral resolution of approximately 0.6 nm. It achieves a spatial resolution of 3.5 km × 7 km (over Seoul at nadir) and a temporal resolution of one hour. The observational domain of GEMS covers 5°S–45°N and 75°E–145°E, delivering 6–10 measurements per day over the Asian region (Kim et al., 2020b).

This study utilizes the GEMS Level 2 NO_2 tropospheric VCD v3.0 product. To ensure data quality, quality control was applied, retaining only pixels where the VCD is greater than zero, the cloud fraction is less than 0.3, and the solar zenith angle is less than 70°. The quality-controlled GEMS data were then regridded to a uniform 0.05° × 0.05° latitude-longitude grid using bilinear interpolation to facilitate spatial alignment with other datasets. GEMS data from January 1, 2023, to December 31, 2023, were used as the training labels for the model, with data of 2024 reserved for additional validation. Furthermore, all the GEMS data mentioned subsequently refer to the nearest whole-hour time point of their average transit time in that area.

https://doi.org/10.5194/essd-2026-443
Preprint. Discussion started: 24 June 2026

2.3 TROPOMI tropospheric NO_2 data

The TROPOspheric Monitoring Instrument (TROPOMI) is an imaging spectrometer onboard the European Space Agency's (ESA) Sentinel-5 Precursor (S5P) satellite, which was launched on October 13, 2017 (Veefkind et al., 2012b; Ialongo et al., 2020). S5P operates in a sun-synchronous polar orbit at an altitude of approximately 824 km, achieving daily global coverage with a local equator crossing time of around 13:30. TROPOMI employs a push-broom imaging technique with a wide swath of 2600 km. Its spectral range covers the ultraviolet, visible, near-infrared, and shortwave infrared bands (270–2385 nm), with the NO_2 retrieval primarily relying on the visible band (405–465 nm) (Geffen et al., 2019) and the cloud retrieval relying on UV/visible/NIR bands (Loyola et al., 2018). The instrument's spatial resolution was enhanced from 7 × 3.5 km^2 to 5.5 × 3.5 km^2 (across-track × along-track) on August 6, 2019 (Liu et al., 2021a), making it the highest-resolution operational sensor for NO_2 monitoring on a polar-orbiting platform.

The TROPOMI NO_2 product has been validated against ground-based Pandora spectrometers, Multi-Axis Differential Optical Absorption Spectroscopy (MAX-DOAS) observations, and aircraft campaigns, demonstrating high accuracy (Griffin et al., 2019; Ialongo et al., 2020; Verhoelst et al., 2021). This study uses the TROPOMI Level 2 tropospheric NO_2 VCD products from 2019 to 2024, with data from 2023 employed for model training. For TROPOMI data, a quality assurance flag (qa_value) greater than 0.75 was used as the filtering criterion. The filtered data were subsequently regridded to the same 0.05° × 0.05° grid using the HARP toolkit (https://github.com/stcorp/harp).

2.4 GOME-2 tropospheric NO_2 data

GOME-2 (Global Ozone Monitoring Experiment-2) is an ultraviolet-visible imaging spectrometer onboard the MetOp series of satellites operated by the European Organisation for the Exploitation of Meteorological Satellites (EUMETSAT). The GOME-2 series consists of three satellites: MetOp-A (launched in October 2006), MetOp-B (launched in September 2012), and MetOp-C (launched in November 2018). GOME-2 has a local overpass time of approximately 09:30 and provides daily global coverage (Munro et al., 2016).

The GOME-2 NO_2 products (Valks et al., 2011) have undergone long-term validation and improvement. Comparison studies with ground-based MAX-DOAS, Pandora observations, and other satellite products have demonstrated good consistency at both global and regional scales (Pinardi et al., 2010; Liu et al., 2019). This study utilizes the GOME-2C Level 2 daily tropospheric NO_2 product provided by EUMETSAT AC-SAF (Hassinen et al., 2016). The data were regridded to a 0.25° × 0.25° resolution using the HARP toolkit, and pixels with a cloud fraction greater than 0.3 were filtered out. This product is primarily used for the cross-comparison and independent validation of the model's prediction results in subsequent chapters. Given the significant difference between GOME-2's overpass time and those of TROPOMI and GEMS, its data offer an independent reference for assessing the diurnal variation of NO_2 and the model's temporal generalization capability.

2.5 ERA5 meteorological reanalysis data

Meteorological conditions play a decisive role in influencing the spatiotemporal heterogeneity of tropospheric NO_2 through physical transport and chemical modulation processes. This study uses the fifth generation of the European Centre for Medium-Range Weather Forecasts (ECMWF) atmospheric reanalysis, ERA5 (Hersbach et al., 2020). This dataset is produced using the Integrated Forecasting System (IFS) Cycle 41r2, which assimilates a vast range of global observations through a 4D-Var data assimilation system. It provides data at a spatial resolution of 0.25° × 0.25° and an hourly temporal resolution. ERA5 has been

https://doi.org/10.5194/essd-2026-443
Preprint. Discussion started: 24 June 2026

widely adopted in atmospheric chemistry research, serving as a meteorological driver for chemical transport models (CTMs), as auxiliary input for satellite retrievals, and as feature variables in machine learning models (Zhang et al., 2025b; Mols et al., 2026).

Both single-level and pressure-level variables from ERA5 were utilized in this study. The single-level variables include boundary layer height (BLH), surface pressure (SP), and total cloud cover (TCC). Boundary layer height is a key physical parameter governing near-surface NO_2 concentrations (Stull, 2012; von Engeln and Teixeira, 2013) and indirectly influences satellite-retrieved tropospheric NO_2 VCDs through the lower-tropospheric contribution to the column. Surface pressure not only indicates the evolution of weather systems but also directly affects the normalization of a priori profiles and the weighting of lower-layer contributions in the calculation of air mass factor (AMF) (Boersma et al., 2007). Total cloud cover modulates the photolysis rate of NO_2 and photochemical equilibrium by altering shortwave radiation reaching the lower atmosphere (van Weele and Duynkerke, 1993), while also being closely linked to precipitation and local thermal circulations (Sfica et al., 2021).For multi-level variables, specific humidity (q), temperature (T), and horizontal wind components (u, v) were extracted at four levels: 500 hPa, 850 hPa, 925 hPa, and 1000 hPa. Lower-level variables can capture thermodynamic and dynamic conditions near NO_2 emission sources, whereas the 500 hPa level represents the large-scale circulation background and vertical transport potential in the mid-troposphere. Temperature and specific humidity jointly determine the thermodynamic conditions and oxidant environment for atmospheric chemical reactions (Mentel et al., 1996; Wang et al., 2020). The wind components provide vector information on the horizontal transport of pollutants. All ERA5 variables used are hourly data at a 0.25° resolution, serving as part of the low-resolution channels input to the model.

2.6 EAC4 reanalysis data

The ECMWF Atmospheric Composition Reanalysis 4 (EAC4) is a core data product of the Copernicus Atmosphere Monitoring Service (CAMS), providing a spatiotemporally consistent reanalysis of global atmospheric composition from 2003 to the present (Inness et al., 2019). EAC4 is based on the atmospheric chemistry module of the ECMWF's IFS and assimilates multi-source satellite observations with model forecasts using a 4D-Var scheme to produce chemically consistent and spatiotemporally complete atmospheric composition fields (Flemming et al., 2017).

This study employs the total column NO_2 (tcno2) variable from EAC4 as an input feature. Although it differs from the satellite-observed tropospheric NO_2 concentration, this product provides a spatiotemporally complete a priori estimate of the NO_2 field, thereby enriching valuable physical prior information available to the model. The original EAC4 product has a temporal resolution of 3 hours and a spatial resolution of 0.75° × 0.75°. To align with the overall framework, EAC4 data were resampled to a 1-hour temporal resolution and a 0.25° × 0.25° spatial resolution using linear interpolation, making it consistent with the ERA5 reanalysis data.

2.7 MCD12C1 land cover data

Land use/land cover (LULC) type is a critical factor influencing the spatial distribution of NO_2. Different land use types correspond to distinct emission source characteristics and intensities: urban and built-up areas concentrate emissions from traffic, industry, and residential activities; agricultural lands are associated with emissions from farm machinery and soil nitrogen cycles; and forests and grasslands are primarily influenced by natural emissions and biomass burning (Lamsal et al., 2013b; Song et al., 2019). Furthermore, land use types indirectly affect the accuracy of satellite retrievals and local meteorological conditions by influencing surface albedo and roughness (Auer, 1978; Noguchi et al., 2014). Consequently, incorporating land use information as a spatial prior helps the model to better understand the heterogeneity of NO_2 spatial patterns.

https://doi.org/10.5194/essd-2026-443
Preprint. Discussion started: 24 June 2026

This study uses the annual MODIS Version 6.1 Climate Modeling Grid (CMG) land cover product, MCD12C1, for the years 2019–2023 (Friedl and Sulla-Menashe, 2022). The Leaf Area Index (LAI)-based classification scheme (LCType3) was selected. Given the mismatch in spatial resolution between MCD12C1 (0.05°) and physical driver fields (0.25°), the land cover data were spatially aggregated to the 0.25° grid by averaging.

2.8 ETOPO 2022 elevation data

Topography is another essential spatial prior variable. Elevation is directly related to atmospheric pressure and air density (Zhou et al., 2009), while topographical variations influence local circulation patterns (e.g., valley and slope winds) and pollutant transport pathways (Gohm et al., 2009). Topography is also closely linked to the spatial distribution of emission sources, as human activities and NO_2 emissions are predominantly concentrated in low-lying plains and basins, whereas emissions are sparse in high-altitude mountains and plateaus (Lamsal et al., 2013b; Yuan et al., 2025). Additionally, terrain elevation affects the calculation of the AMF in satellite retrievals, with higher uncertainty typically observed over high-altitude areas (Boersma et al., 2011b). Therefore, integrating topographical information into the model enhances its predictive capability for NO_2 distribution, especially in regions with complex terrain.

This study utilizes the Earth TOPOgraphy (ETOPO) 2022 global relief model (NOAA National Centers for Environmental Information, 2022). As the latest version in the ETOPO series, it integrates multi-source topographic and bathymetric data, including satellite altimetry, shipborne sonar, airborne gravity, and terrestrial digital elevation models, to provide a high-resolution global relief dataset for land and ocean (MacFerrin et al., 2025). This study utilizes the 60-arc-second resolution version, which was resampled to a 0.25° × 0.25° resolution via spatial aggregation (averaging) to align with the grid of the other physical variables.

3. Methodology

3.1 Multi-source data integration framework

This study integrates multi-source datasets with heterogeneous origins, spatiotemporal resolutions, and physical units, constructing an input tensor system comprising 2 high-resolution satellite channels, 33 low-resolution feature channels, and 1 label channel. Table 2 systematically summarizes the source, original resolution, physical significance, and normalization strategy of all input variables.

Table 2: Summary of input variables for PhysNorm-Net.

Source	Variable Name	Abbreviation	Spatial Resolution	Temporal Resolution	Channels	Normalization Method
TROPOMI	Tropospheric NO_2 VCD	TROPOMI NO_2	0.05°	daily	1	Log+Z-Score
	mask	mask	0.05°	daily	1	/
GEMS	Tropospheric NO_2 VCD	GEMS NO_2	0.05°	hourly	1 (label)	Log+Z-Score
EAC4	NO_2 Total Column	tcno2	0.25°	hourly	1	Z-Score

https://doi.org/10.5194/essd-2026-443
Preprint. Discussion started: 24 June 2026

ERA5	Surface Pressure	sp	0.25°	hourly	1	Z-Score
	Total Cloud Cover	tcc			1	Z-Score
	Boundary Layer Height	blh			1	Z-Score
	Specific Humidity	q			4	Z-Score
	Temperature	T			4	Z-Score
	U-component of wind	u			4	Z-Score
	V-component of wind	v			4	Z-Score
ETOPO2022	Digital Elevation Model	DEM	0.25°	/	1	Min-Max
MCD12C1	Land Cover Type	/	0.25°	yearly	11	Convert to decimals
Computed	Cosine of Solar Zenith Angle	SZA	0.25°	hourly	1	/

Note: The 4 channels for ERA5 multi-level variables correspond to 1000, 925, 850, and 500 hPa pressure levels. The 11 channels for MCD12C1 represent the 11 land cover types.

To ensure numerical stability during neural network training and eliminate the influence of dimensional discrepancies on gradient propagation, differentiated normalization strategies were tailored to the characteristics of each variable type. Prior to normalization, the 2023 dataset was randomly partitioned by date into training (256 days), validation (54 days), and test (55 days) sets.

The probability distribution of tropospheric NO_2 column densities exhibits a pronounced positive skew, with several orders of magnitude separating high-value tails (corresponding to pollution events) from background concentrations. A direct linear scaling would compress the information content of high-concentration pixels while disproportionately amplifying minor variations in low-concentration regions, thereby hindering the model's ability to learn the spatial features of both pollution hotspots and background areas. To address this, TROPOMI and GEMS tropospheric NO_2 VCDs were first scaled by a factor of 10^{-15} (converting to units of Pmolec/cm^2), followed by logarithmic transformation and Z-score normalization:

$$x_{\log} = \ln\left(x_{\text{trop}} + \epsilon\right) \tag{1}$$

$$x_{\text{norm}} = \frac{x_{\log} - \mu_{\log}}{\sigma_{\log}} \tag{2}$$

Here, ϵ is a small constant to prevent undefined logarithms for zero values, while $\mu_{\log}$ and $\sigma_{\log}$ represent the global mean and standard deviation of the log-transformed training data, respectively. The logarithm transform effectively compresses the dynamic range of the data, making its distribution more Gaussian-like while preserving the relative relationships between concentration gradients. The subsequent Z-score standardization centers the data and scales it to a standard deviation of one, aligning it with the standard input assumptions of deep neural networks (LeCun et al., 2012).

https://doi.org/10.5194/essd-2026-443
Preprint. Discussion started: 24 June 2026

For ERA5 and EAC4 reanalysis variables, Z-score normalization was uniformly applied:

$$x' = \frac{x - \mu}{\sigma} \tag{3}$$

Where μ and σ are the spatiotemporal statistics of each variable computed over the training set. It is emphasized that all normalization statistics are derived exclusively from the training set and subsequently applied to the validation and test sets to strictly prevent data leakage.

Since DEM data possess well-defined physical boundaries (from sea level to the highest peak) and its absolute values carry physical meaning, a min-max normalization was applied to preserve this characteristic while mapping values to the [0, 1] interval:

$$z' = \frac{z - z_{\min}}{z_{\max} - z_{\min}} \tag{4}$$

Where $z_{\max}$ and $z_{\min}$ are the global minimum and maximum DEM values.

Land use data from MCD12C1 are provided as area fractions (original values as percentages from 0–100); these were directly converted to decimals in the [0, 1] range by dividing by 100. Normalization of both DEM and land use data was performed prior to spatial resampling.

For temporal encoding, while spatiotemporal prediction tasks typically employ periodic functions (e.g., sine/cosine transforms) to explicitly embed hour, day, or year cycles, such purely mathematical encodings may lack a direct connection to atmospheric physical processes. Therefore, this study proposes using the cosine of the solar zenith angle ($\cos(\theta_{\mathrm{SZA}})$) as a substitute for conventional time encoding. For a given UTC time, regions at different longitudes experience different local solar times and corresponding SZAs. The SZA implicitly encodes the longitude-time coupling, enabling the model to understand local illumination conditions without needing to learn complex time zone conversion logic. Furthermore, the SZA reflects both diurnal and seasonal variations (depending on solar declination), allowing a single variable to represent periodicity across multiple time scales and reducing input feature redundancy.

The calculation process is as follows: based on the UTC timestamp and the central coordinates of the region, the solar elevation angle (α) is first computed using a solar position algorithm (Reda and Andreas, 2004), from which the solar zenith angle (θ_{SZA}) is derived:

$$\theta_{\mathrm{SZA}} = 90° - \alpha \tag{5}$$

To constrain input values within the numerical range preferred by neural networks, the cosine is taken:

$$f_{\mathrm{SZA}} = \cos(\theta_{\mathrm{SZA}}) \tag{6}$$

This value approaches 0 near sunrise/sunset and approaches 1 at solar noon in tropical regions (or less than 1 at mid-to-high latitudes), offering intuitive physical interpretation. Given that the spatial resolution of data such as EAC4 is 0.25°, corresponding to a grid scale of approximately 25–30 km, the spatial variation of the SZA within this scale is negligible (< 0.1°). Therefore, f_{SZA} is treated as a spatially uniform field and appended to the low-resolution tensor.

3.2 Overall architecture of PhysNorm-Net

Let the high-resolution TROPOMI NO_2 observations be denoted as $X_{\mathrm{obs}} \in \mathbb{R}^{H \times W}$. Due to cloud cover, aerosol contamination, and sensor swath gaps, the observation field is spatially sparse. Therefore, a binary mask $M \in \{0,1\}^{H \times W}$ is introduced to mark the locations of valid pixels (1 for valid, 0 for missing). Concurrently, to incorporate the dynamic constraints of atmospheric transport and dispersion, a set of spatiotemporally aligned, low-resolution physical and topography data is utilized, denoted as $P \in \mathbb{R}^{h \times w \times C}$, where $h < H$, $w < W$, and C is the number of physical variable channels. The objective of this study is to learn a nonlinear

https://doi.org/10.5194/essd-2026-443
Preprint. Discussion started: 24 June 2026

Open Access Earth System Science Data Discussions

mapping function $\mathcal{F}$ that infers the complete, high-spatiotemporal-resolution NO_2 field $\hat{Y}$ by fusing the sparse observations with the dense physical prior:

$$\hat{Y} = \mathcal{F}(\mathrm{X}_{\mathrm{obs}}, P, M) \tag{7}$$

The challenge inherent in this problem lies in the significant modality gap between X_{obs} and P: the former contains high-frequency spatial textures but is incomplete, while the latter is physically continuous but spatially coarse. To address this multi-modal fusion challenge, the PhysNorm-Net is designed. As illustrated in Figure 1, the network's main body inherits the classic U-Net architecture (Ronneberger et al., 2015), comprising a contracting path (encoder) and an expansive path (decoder), with skip connections to preserve multi-scale features. However, two critical asymmetric modifications are introduced to the standard U-Net to accommodate irregularly missing data and to integrate physical constraints:

The Main Observation Stream, which forms the U-Net backbone, is responsible for extracting multi-scale features from the spatially incomplete TROPOMI field. Unlike traditional Convolutional Neural Networks (CNNs) that use standard convolutional layers, this stream is constructed from a stack of Partial Convolution layers. This enables the network to adaptively handle data missing in arbitrary shapes, progressively in-painting the feature maps during the encoding process.

The Physics-Conditional Stream operates as a parallel feature extractor, deriving latent physical information from the low-resolution data. This stream employs a deep residual network (ResNet) structure to prevent gradient vanishing during deep feature extraction and to ensure the effective propagation of physical information.

During the decoding (upsampling) phase, features from the physics stream are not simply concatenated with the observation features. Instead, they are used to dynamically modulate the statistical distribution of the observation features through a novel Physics-Aware Normalization (PhysNorm) module. This conditional affine transformation fuses the two streams of information to reconstruct the high-resolution tropospheric NO_2 field. This design ensures that the generated pollutant concentration field not only retains the fine details from the satellite observations but also adheres macroscopically to the prevailing meteorological dispersion patterns.

https://doi.org/10.5194/essd-2026-443
Preprint. Discussion started: 24 June 2026

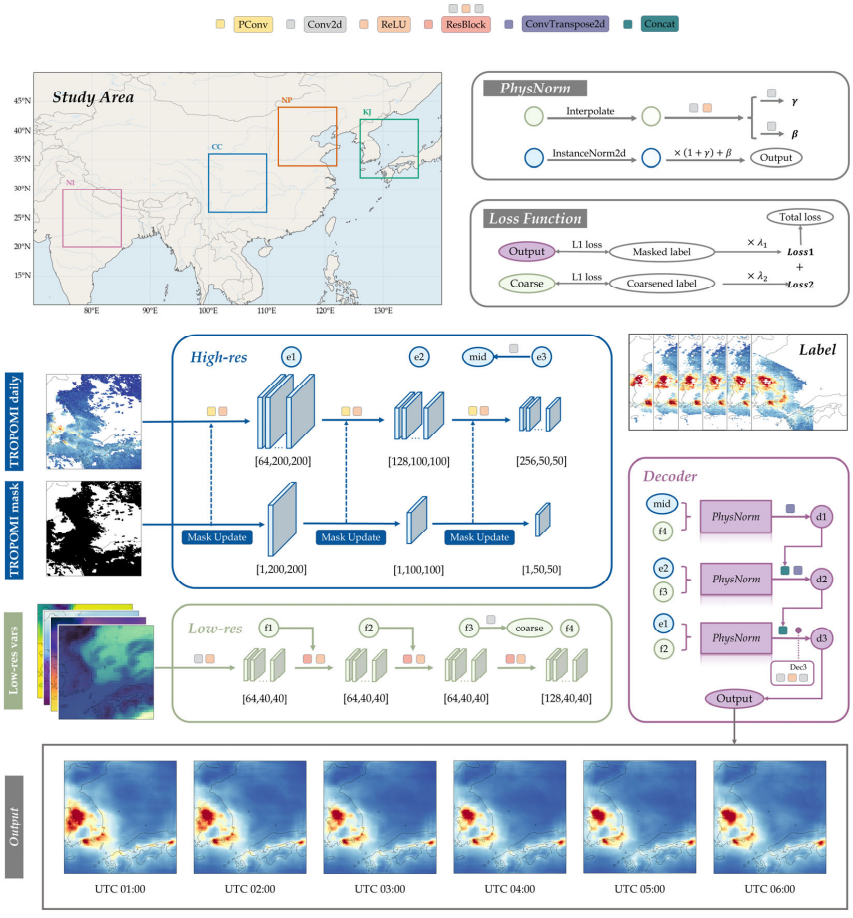

Figure 1: Architecture diagram of PhysNorm-Net.

3.3 Observation encoding via Partial Convolution

Spatial gaps in satellite remote sensing imagery exhibit high irregularity, with patterns, areas, and locations varying across samples. Standard convolution operations implicitly assume all input pixels are valid and incorporate padded values (e.g., zeros or mean-filled values) in missing regions into feature calculations. This leads to the contamination of features from valid areas by missing areas, an error that propagates and diffuses throughout the feature map as network depth increases. To resolve this issue, this study adopts the Partial Convolution (PConv) layer, proposed by Liu et al. (2018), as the fundamental operator in the encoder. The core mechanism of PConv is to perform convolution exclusively on the valid pixels defined by a mask and to re-weight the result based on the proportion of valid pixels.

Assume the input feature at layer l is $X^{(l)}$, the corresponding binary mask is $M^{(l)}$, the convolution kernel is W, and the bias is b. The partial convolution output at position (i, j) is computed as:

https://doi.org/10.5194/essd-2026-443
Preprint. Discussion started: 24 June 2026

$$x'_{(i,j)} = \begin{cases} W^T\left(X^{(l)} \odot M^{(l)}\right)_{(i,j)} \cdot \dfrac{\text{sum}(1)}{\text{sum}(M^{(l)})_{(i,j)}} + b, & \text{if sum}\left(M^{(l)}\right)_{(i,j)} > 0 \\ 0, & \text{otherwise} \end{cases} \quad (8)$$

Here, $\odot$ denotes element-wise multiplication, $sum(1)$ is the total number of pixels in the convolutional window, and $sum\left(M^{(l)}\right)_{(i,j)}$ is the number of valid pixels within that window. The scaling factor $\frac{sum(1)}{sum(M^{(l)})_{(i,j)}}$ automatically corrects for the reduction in signal strength caused by the diminished amount of valid information. Simultaneously, the mask is updated after each layer: a position in the next layer's mask is marked as valid if at least one valid pixel existed within its receptive field in the current layer. This hierarchical update mechanism enables valid information to propagate layer-by-layer toward missing regions as network depth increases, providing the decoder with structurally complete semantic features.

Specifically, the high-resolution encoder employs a three-stage downsampling architecture. The first stage uses a 7×7 large-kernel convolution (64 channels) to rapidly expand the receptive field while preserving the original resolution, which is suitable for capturing medium-scale NO_2 spatial structures. The subsequent two stages use 3×3 convolutions (128 and 256 channels, respectively) to perform 2x downsampling. The feature maps and updated masks at each stage are preserved for use in the decoder via skip connections.

3.4 Residual encoding of physical priors

The physical prior encoding module is tasked with extracting a hierarchical feature representation of the atmospheric state from the low-resolution tensor $P \in \mathbb{R}^{h\times w\times C}$. The design objectives for this module are: (a) to capture the nonlinear mapping relationships between meteorological fields, surface characteristics, and NO_2 distribution; and (b) to generate multi-level physical features for fusion at different resolution scales in the decoder. Traditional deep convolutional networks, after alternating between multiple layers of linear convolution and nonlinear activation, are prone to gradient degradation, which can lead to the over-abstraction or even loss of spatially continuous information present in the original meteorological data. Therefore, this module adopts a residual network (ResNet) architecture, consisting of an initial convolutional layer followed by three residual blocks. The introduction of residual connections alleviates gradient vanishing in deep networks (He et al., 2015) while facilitating the learning of incremental functions near identity mappings from input to output. This network produces three levels of physical feature maps $\left\{F_{\text{phy}}^{(1)}, F_{\text{phy}}^{(2)}, F_{\text{phy}}^{(3)}\right\}$ (with 64, 64, and 128 channels, corresponding to f2, f3, f4 in Figure 1), which encode hierarchical information from raw meteorological variables to abstract physical patterns.

Specifically, the low-resolution input is first mapped to a latent feature space via an initial convolutional layer, followed by deep feature extraction through a stack of residual blocks. If the input feature to the k-th residual block is $F_{\text{phy}}^{(k-1)}$, the feature propagation process can be described as:

$$F_{\text{phy}}^{(k)} = \text{ReLU}\left(F_{\text{phy}}^{(k-1)} + \mathcal{R}_k\left(F_{\text{phy}}^{(k-1)}\right)\right) \quad (9)$$

where $\mathcal{R}_k$ represents the residual mapping composed of two consecutive convolutional layers with embedded nonlinear activation functions. The identity mapping term $F_{\text{phy}}^{(k-1)}$ allows fundamental physical information provided by the low-resolution branch to be directly transmitted to deeper network layers. The residual term $\mathcal{R}_k(\cdot)$ is consequently forced to learn only refinements (or perturbations). The physical prior encoder does not merely output a single global feature vector but extracts multi-scale hierarchical features under different receptive fields. These features are then routed to and precisely aligned with the PhysNorm modules at different depths of the high-resolution decoder.

https://doi.org/10.5194/essd-2026-443
Preprint. Discussion started: 24 June 2026

Additionally, this module includes an auxiliary prediction head (a 1×1 convolution layer) that directly predicts a coarse-resolution NO_2 field $\hat{Y}_{\text{coarse}}$ from the intermediate feature layer $F_{\text{phys}}^{(2)}$. This auxiliary output provides an additional supervisory signal during training (detailed in Section 3.6), ensuring that the physical features possess direct predictive capability for NO_2 concentrations.

3.5 Physics-Aware Normalization (PhysNorm) module and multi-scale decoder

A core challenge of this research is how to effectively fuse low-resolution physical information during the decoder's process of recovering high-resolution details. Traditional fusion methods, such as concatenation or addition, treat physical information as an additional feature channel, relying on the network to implicitly learn its relationship with satellite observations. This often leads to the deep learning network prioritizing the observational data and ignoring the physics stream, causing the model to degrade into image interpolation. Inspired by Spatially-Adaptive (De)normalization (SPADE) from the image generation domain (Park et al., 2019), this study proposes the Physics-Aware Normalization module. This module treats the meteorological field as an environmental context that dynamically modulates the normalized statistics of the satellite feature map via an affine transformation. The workflow of PhysNorm involves three main steps:

Destylization: First, the input satellite feature map (F_{sat}, corresponding to mid, e2, e1 in Figure 1) undergoes parameter-free Instance Normalization (IN). This step removes biases in absolute concentration that are specific to a particular time and region by subtracting the mean and dividing by the standard deviation, thereby retaining the pure relative structural information:

$$\hat{F}_{\text{sat}} = \frac{F_{\text{sat}} - \mu(F_{\text{sat}})}{\sigma(F_{\text{sat}})} \tag{10}$$

Parameter Mapping: Using the multi-scale features (F_{phy}) extracted by the physics encoder, two separate shallow convolutional networks, ϕ_γ and ϕ_β, learn the scaling (γ) and shifting (β) coefficients corresponding to the specific meteorological conditions:

$$\gamma = \phi_\gamma(F_{\text{phy}}), \beta = \phi_\beta(F_{\text{phy}}) \tag{11}$$

Here, γ and β are tensors of the same spatial dimensions as $\hat{F}_{\text{sat}}$.

Physics Injection: The learned parameters are then used to modulate the normalized features:

$$F_{\text{out}} = \hat{F}_{\text{sat}} \cdot (1 + \gamma) + \beta \tag{12}$$

The scaling factor γ and shifting factor β control the local concentration contrast and background level, respectively. For instance, under conditions of strong winds and high dispersion, where the pollutant distribution tends to be more uniform, the model would predict smaller γ values to suppress local peaks. In areas with a low boundary layer height or high emissions, the model would generate positive β values to holistically elevate the predicted concentrations in that region. Through PhysNorm, the model can be compelled to rely on the physical state (low-resolution input) to determine the numerical range and distribution intensity of the final output, fundamentally resolving the information imbalance issue in modality fusion.

The decoder adopts a symmetric three-stage upsampling architecture, progressively recovering spatial resolution via transposed convolutions. PhysNorm is deployed at each decoder stage, modulated by the deep, intermediate, and shallow features from the physical prior module, respectively. This hierarchical design allows physical information of varying abstraction levels to act on corresponding spatial scales: deep features modulate weather-scale patterns, while shallow features modulate variations at the local scale.

https://doi.org/10.5194/essd-2026-443
Preprint. Discussion started: 24 June 2026

In this architecture, the PhysNorm module modulates encoder features prior to concatenation. The final output layer is a lightweight convolutional head (two 3×3 convolutional layers, 128→32→1 channels), which maps the fused features to a single-channel NO_2 prediction field.

3.6 Dual-task loss function

To maintain physical consistency while ensuring high-resolution reconstruction accuracy, this study proposes a dual-task constrained loss function. The total loss is a linear combination of a fine-grained reconstruction loss and a coarse-grained physical consistency loss:

$$\mathcal{L}_{\text{total}} = \lambda_1 \mathcal{L}_{\text{fine}} + \lambda_2 \mathcal{L}_{\text{coarse}} \tag{13}$$

The fine-grained reconstruction loss ($\mathcal{L}_{\text{fine}}$) supervises the final high-resolution output of the U-Net. Since the ground truth labels (GEMS data) themselves contain missing values, the loss is computed only over valid pixels. An L1 loss is adopted to enhance robustness against outliers in satellite data.

The physical consistency loss ($\mathcal{L}_{\text{coarse}}$) supervises the coarse-resolution prediction from the physical prior module. The GEMS labels are downsampled to the low-resolution grid after handling invalid values, and the loss is computed in the same masked L1 form. This auxiliary task ensures that the physical features possess direct predictive capability for NO_2 and provides a more direct gradient signal to the shallow layers of the network, alleviating the gradient dilution problem in deep networks. In our setup, both λ_1 and λ_2 are set to 1.0.

3.7 Evaluation metrics

This study employs multiple evaluation metrics to assess model performance, all of which are calculated based on valid observation pixels. Detailed descriptions follow:

The coefficient of determination (R^2) measures the extent of the variance between predictions and original observations. It is defined as:

$$R^2 = 1 - \frac{\sum_{i=1}^{n}(y_i - \hat{y}_i)^2}{\sum_{i=1}^{n}(y_i - \bar{y})^2} \tag{14}$$

where y_i and $\hat{y}_i$ are the observed and predicted values for the i-th sample, $\bar{y}$ is the mean of the observed values, and n is the total number of samples. R^2 ranges from $-\infty$ to 1, with values closer to 1 indicating a better fit. To evaluate the statistical significance of R^2, the F-test is employed to compute its associated probability (p-value). The F-statistic is defined as:

$$F = \frac{R^2/k}{(1 - R^2)/(n - k - 1)} \tag{15}$$

where k is the number of independent variables in the regression model. Under the null hypothesis ($R^2_{true} = 0$), F follows an F-distribution with degrees of freedom $(k, n - k - 1)$. The p-value is computed via the survival function of the F-distribution, and p<0.05 indicates that R^2 is significantly different from zero at the 95% confidence level.

When validating against another independent source (e.g., the LEO satellite GOME-2), which may have inherent differences in retrieval algorithms and observation geometries, this study uses the Pearson correlation coefficient (R) as the core metric for cross-validation:

$$R = \frac{\sum_{i=1}^{n}(y_i - \bar{y})(\hat{y}_i - \bar{\hat{y}})}{\sqrt{\sum_{i=1}^{n}(y_i - \bar{y})^2}\sqrt{\sum_{i=1}^{n}(\hat{y}_i - \bar{\hat{y}})^2}} \tag{16}$$

https://doi.org/10.5194/essd-2026-443
Preprint. Discussion started: 24 June 2026

where $\bar{\hat{y}}$ is the mean of predicted values. Pearson R ranges from −1 to 1, and values closer to ±1 indicate stronger linear correlation.

Root Mean Square Error (RMSE) quantifies the overall magnitude of the prediction error. It is defined as:

$$RMSE = \sqrt{\frac{1}{n}\sum_{i=1}^{n}(y_i - \hat{y}_i)^2} \quad (17)$$

RMSE has the same units as the observations (Pmolec/cm^2), facilitating a direct assessment of the error's actual magnitude.

Mean Absolute Error (MAE) measures the average magnitude of the errors, assigning equal weight to each error. It is defined as:

$$MAE = \frac{1}{n}\sum_{i=1}^{n} | y_i - \hat{y}_i | \quad (18)$$

Compared to RMSE, MAE is more robust to outliers. Using both metrics can reveal characteristics of the error distribution: a RMSE value significantly larger than the MAE suggests the presence of a few samples with large errors.

Normalized Mean Bias (NMB) normalizes the mean bias relative to the mean of the observations, enabling comparable assessments across different regions and time periods. It is defined as:

$$NMB = \frac{\sum_{i=1}^{n}(\hat{y}_i - y_i)}{\sum_{i=1}^{n} y_i} \times 100\% \quad (19)$$

NMB expresses the relative degree of systematic bias as a percentage, eliminating the influence of varying absolute NO_2 concentrations across different regions or seasons.

4. Results

4.1 Overall dataset accuracy and spatiotemporal consistency

To comprehensively evaluate the model's ability to predict hourly tropospheric NO_2, Figure 2 presents the overall scatter density plots for the training, validation, and test sets. The predicted dataset achieved high prediction accuracy across all three sets, with R^2 values of 0.939, 0.882, and 0.889, respectively (all p-values < 0.01). Furthermore, during the training and testing process involving tens of millions of samples, the performance metrics on the validation and test sets were highly consistent, with no significant signs of overfitting. This indicates that the designed PhysNorm-Net model can effectively learn the non-linear mapping relationship between multi-source physical drivers and pollutant concentrations.

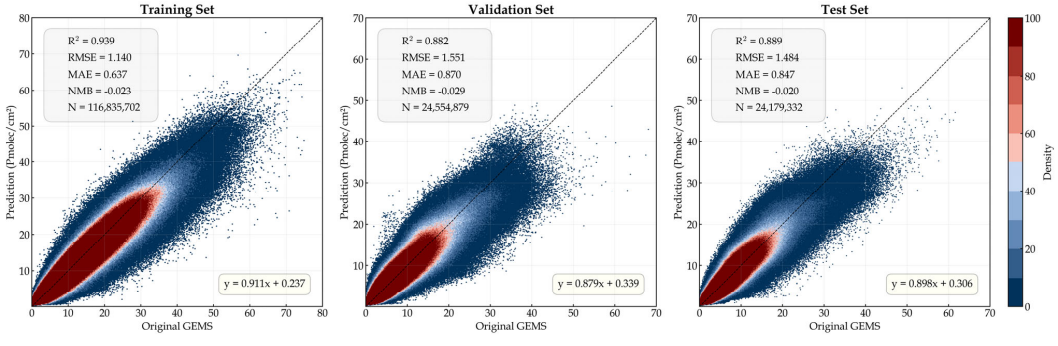

Figure 2: Scatter density plots of model predictions versus original GEMS observations.

https://doi.org/10.5194/essd-2026-443
Preprint. Discussion started: 24 June 2026

Notably, the predicted dataset does not show a systematic underestimation or overestimation trend, except for a slight underestimation in regions with high tropospheric NO_2 column densities (>40 Pmolecules/cm^2). This phenomenon is relatively common in current deep learning-based atmospheric remote sensing retrieval studies (Wei et al., 2021). The main reasons are twofold: first, the L1 loss functions used for model optimization tend to fit the global mean, with a relatively insufficient penalty weight for extreme high values; second, high-concentration samples constitute a very small fraction of the overall data distribution and often correspond to local, sudden emission events or adverse stagnant meteorological conditions, which low-resolution data cannot fully capture. Nevertheless, considering that the core concentration range of tropospheric NO_2 accounts for the vast majority of samples, the dataset demonstrates high reliability in this range, meeting the needs for regional air quality assessment and spatiotemporal evolution analysis.

Regarding spatial distribution details, Figure 3 uses April 26, 2023, as an example to show a single-day spatial comparison across the four typical regions. It is visually evident that the predicted dataset not only successfully fills large data gaps caused by factors like cloud cover but also accurately reproduces the spatial patterns of the original observations and the locations of heavy pollution plumes. In some local areas with complex terrain or dense emission sources (e.g., urban clusters in the NP region), the concentration gradients in the predictions are slightly smoother compared to the original high-resolution satellite observations. This is due to an unavoidable spatial smoothing effect introduced by the physical prior module when fusing the 0.25° physical driving fields with the 0.05° remote sensing data. However, this trade-off effectively eliminates non-physical abrupt changes in the original satellite products caused by retrieval noise and surface albedo errors, while also significantly mitigating common sensor striping artifacts. As a result, the final generated spatial distribution retains sufficiently accurate local hotspot information while adhering to the physical laws of atmospheric diffusion and transport.

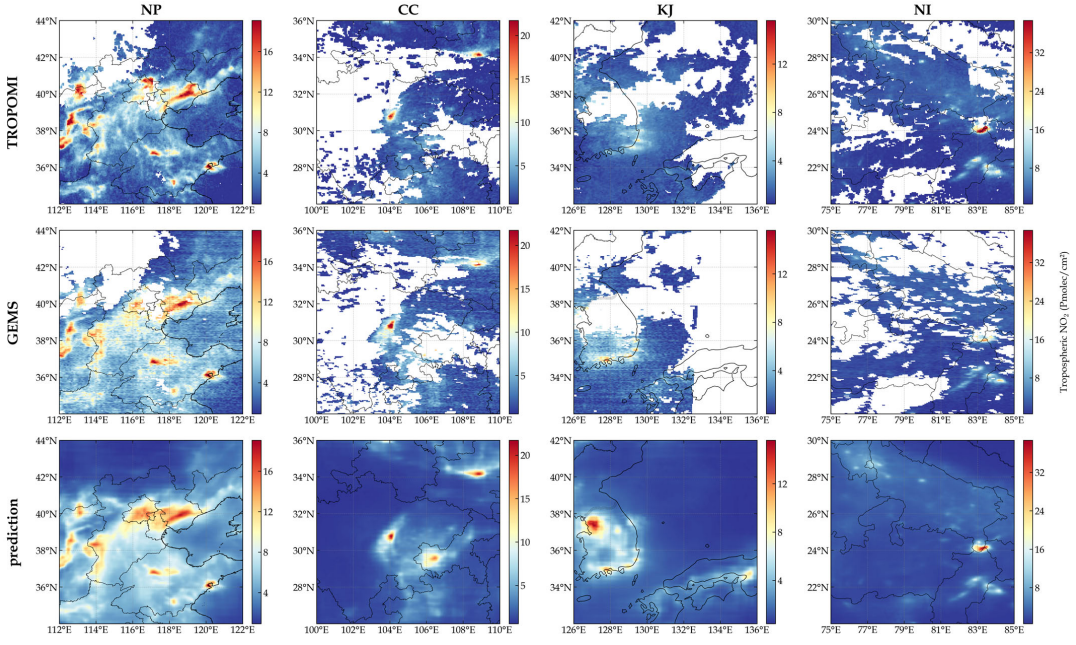

Figure 3: Comparison of single-day spatial distributions of NO_2 concentration from TROPOMI, GEMS, and model predictions on April 26, 2023.

https://doi.org/10.5194/essd-2026-443
Preprint. Discussion started: 24 June 2026

Figure 4 shows the complete hourly GEMS observations and model predictions from 23:00 (UTC) on January 9, 2023 to 08:00 (UTC) on January 10, 2023, clearly demonstrating that the model not only has the ability to fill spatial gaps but also can predict the complete observation time series, thereby obtaining a more coherent dynamic change process.

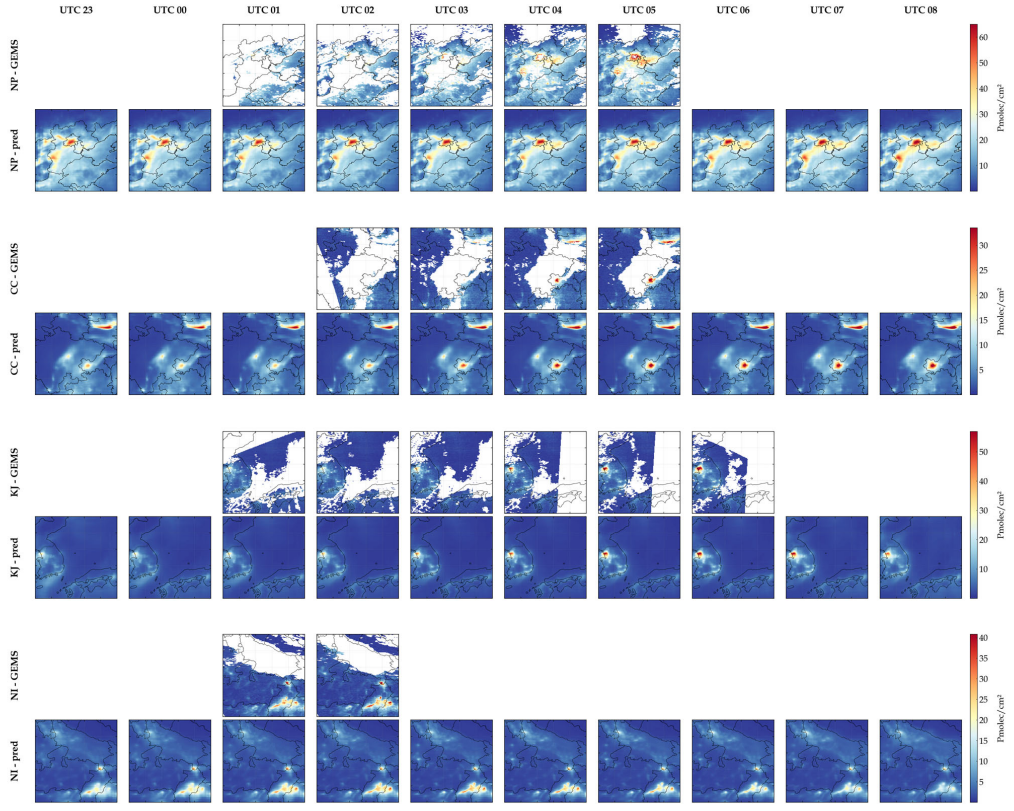

Figure 4: Hourly spatial distributions of NO_2 concentration from GEMS, and model predictions.

To further validate the model's temporal extrapolation capability and long-term application potential, this study applied the model to the data of 2024, which was not involved in any training phase, for independent validation. The performance was compared by region with that of 2023, and the results are shown in Table 3.

Table 3: Comparison of model performance on 2023 and 2024 datasets by region.

Metric	NP		CC		KJ		NI	
	2023	2024	2023	2024	2023	2024	2023	2024
R^2	0.921	0.855	0.879	0.771	0.897	0.817	0.819	0.650
RMSE	1.722	2.339	0.829	1.006	0.884	1.017	1.096	1.403
MAE	1.055	1.461	0.507	0.610	0.492	0.571	0.561	0.815
NMB	-0.016	0.076	-0.023	0.119	-0.035	0.098	-0.041	0.226

The results show that the model maintained robust predictive performance on the 2024 data across all regions. For instance, R^2 values for NP and KJ remained above 0.81. Although there is a slight decline in evaluation metrics (e.g., lower R^2, higher

https://doi.org/10.5194/essd-2026-443
Preprint. Discussion started: 24 June 2026

RMSE) in the cross-year validation compared to the internal test set, this is within a reasonable and expected range. On one hand, fluctuations in socioeconomic activities and the implementation of environmental policies may have caused objective inter-annual baseline shifts in regional anthropogenic emissions in 2024. On the other hand, inter-annual variability in meteorological fields and extreme weather events can also increase the difficulty of extrapolation for data-driven models (Palma et al., 2026). Additionally, the number of labels that GEMS can provide in NI is less than in other regions, which may limit the model's generalization ability, leading to a more pronounced decline in accuracy (R^2 dropping from 0.819 to 0.650).

Despite challenges such as baseline emission shifts and inter-annual meteorological disturbances, the overall reliable predictive performance of the model on the 2024 dataset strongly demonstrates that the deep learning framework has learned the intrinsic dynamic evolution principles of atmospheric physics and chemistry, rather than merely memorizing the data distribution of a specific year. This indicates that the model has significant potential and value for extension to longer time series, such as historical scene reconstructions or future scenario predictions.

4.2 Assessment of spatial hotspot capture and historical reconstruction capability using GOME-2

In order to evaluate the hotspot reconstruction capability and historical prediction accuracy of the dataset predicted by PhysNorm-Net, this section introduces the GOME-2 instrument as a completely independent reference object.

Figure 5 selects typical cases from the four study regions to demonstrate the dataset's capability in reconstructing NO_2 spatial distributions and capturing hotspots during the morning. The dataset predicted by PhysNorm-Net exhibit high spatial completeness and continuity in all cases, successfully capturing morning concentration hotspots that TROPOMI failed to observe effectively. Specifically, in Figure 5(a), the prediction clearly reconstructs the extensive high-value area stretching across the Beijing-Tianjin-Hebei region to Shandong and Henan. This accurately captures the morning NO_2 accumulation caused by the superposition of industrial emissions and rush-hour traffic, and this spatial pattern is highly consistent with both GOME-2 observations and the valid GEMS pixels. In Figure 5(b), the prediction not only fills these gaps but also restores the pollution hotspots centered around the three major cities of Chengdu, Chongqing, and Xi'an. Similar high-fidelity reconstruction is also evident in Figure 5(c) for the Seoul metropolitan core area, and in Figure 5(d) for areas including New Delhi and the junction of Chhattisgarh and Odisha states. These findings demonstrate that the dataset predicted by PhysNorm-Net can not only perform spatiotemporal continuous reconstruction but also realistically reconstruct missed NO_2 hotspots.

https://doi.org/10.5194/essd-2026-443
Preprint. Discussion started: 24 June 2026

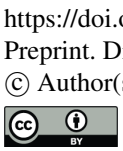

Open Access Earth System Science Data Discussions

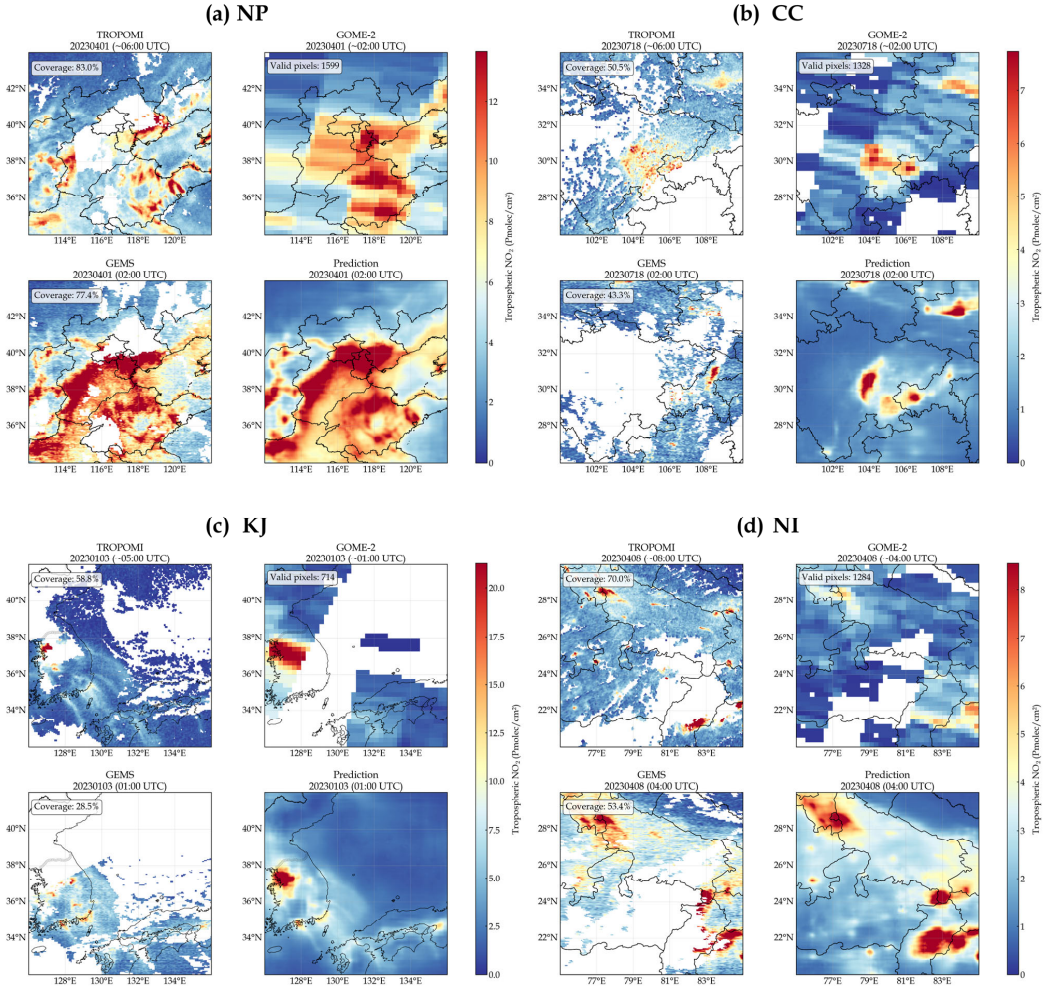

Figure 5: Comparison of tropospheric NO_2 spatial distributions from TROPOMI, GOME-2, GEMS, and model predictions at the GOME-2 overpass time for the four study regions.

Figure 6 displays the validation results of the predictions and original GEMS against GOME-2C from 2019 to 2024, across the four study regions and at the combined all-region scale. Since GEMS data are only available for 2023–2024, the comparison for 2019–2022 is only shown for predictions versus GOME-2C.

https://doi.org/10.5194/essd-2026-443
Preprint. Discussion started: 24 June 2026

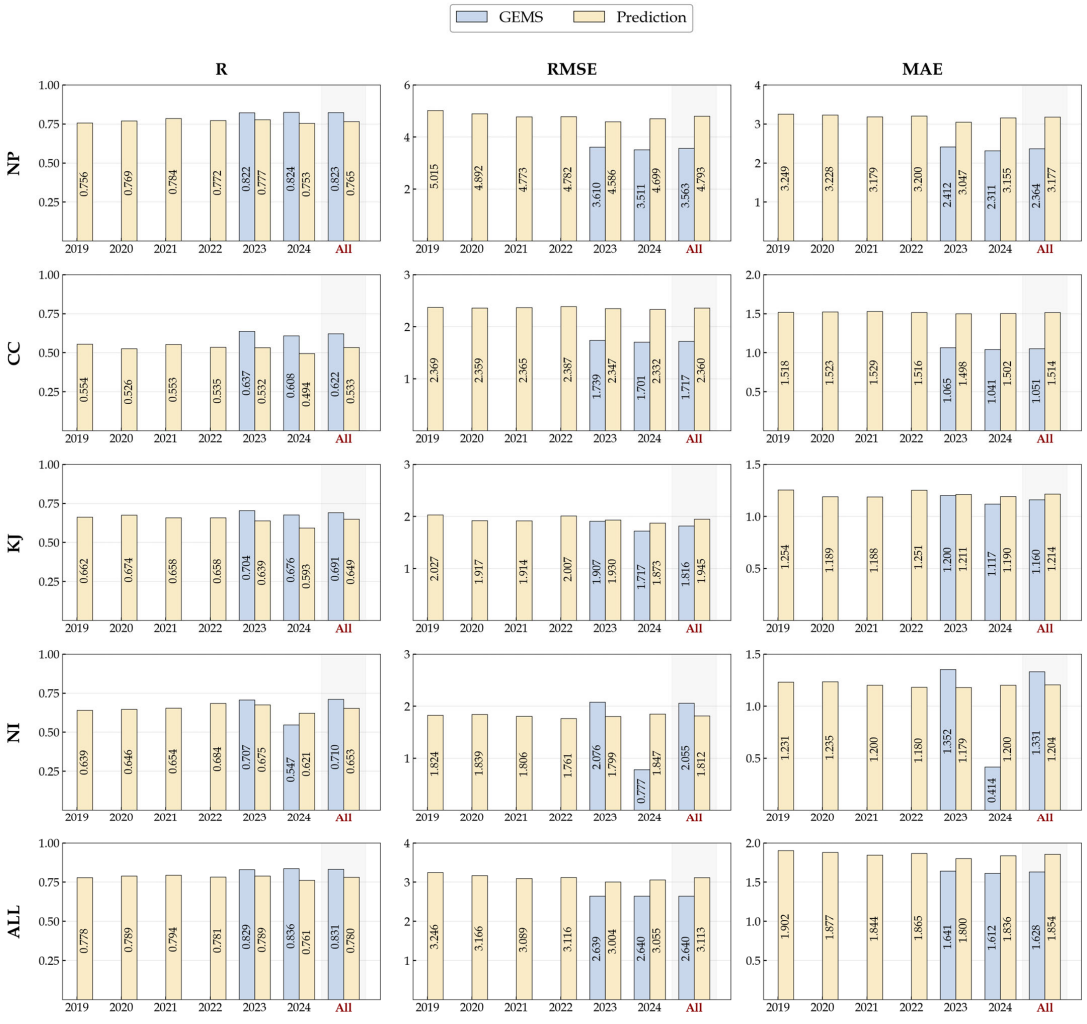

Figure 6: Annual and overall validation results of GEMS and predictions against GOME-2C for each region.

At the all-region scale, the predictions exhibit good inter-annual stability from 2019 to 2024. The annual R for the four combined regions ranges from 0.76 to 0.79, with the RMSE stable within 3.00–3.25 Pmolec/cm^2, and the MAE maintained between 1.80–1.90 Pmolec/cm^2. For the entire six-year period, the overall statistics for predictions against GOME-2C are R = 0.780, RMSE = 3.113 Pmolec/cm^2, and MAE = 1.854 Pmolec/cm^2. Notably, during the 2019–2022 retrospective period, the overall correlation and error levels are comparable to those of 2023–2024, indicating that the dataset predicted by the model has good stability in temporal extrapolation and does not show significant performance degradation when backtracking to non-training years.

At the regional scale, different regions exhibit clear differences. The NP region shows the highest correlation, with a six-year combined R of 0.765 for the predictions, but it also has the largest error magnitude, with RMSE and MAE of 4.794 and 3.177 Pmolec/cm^2, respectively. This suggests that the dataset can effectively capture the dominant structure of NO_2 spatial variations in the North China Plain but is accompanied by larger absolute errors in the context of high values and strong gradients. In contrast,

https://doi.org/10.5194/essd-2026-443
Preprint. Discussion started: 24 June 2026

the CC region exhibits the lowest correlation, with a multi-year combined R of only 0.533 for the predictions, while its RMSE and MAE are 2.360 and 1.514 Pmolec/cm^2, respectively. This indicates that although the absolute error is not high, the spatial consistency is relatively weak in this region. The KJ and NI regions have relatively low overall error levels. The predicted RMSE and MAE for the KJ region are 1.945 and 1.214 Pmolec/cm^2, and for the NI region, they are 1.812 and 1.204 Pmolec/cm^2. The R for both regions is approximately 0.65, indicating that the dataset maintains a relatively stable fitting ability in low-to-medium concentration backgrounds.

In the 2023–2024 period when GEMS observations are available, Figure 6 further validates the high consistency and comparability between the predictions and the GEMS products. At the all-region scale, the correlation of GEMS with GOME-2C (R = 0.829–0.836) indeed shows a slight advantage, while the predictions' R value for the same period also reaches a high level of 0.761–0.789. This demonstrates that the output dataset has successfully internalized and inherited the capability of GEMS data to capture large-scale NO_2 spatial variability. A detailed regional comparison further highlights the robust performance of the predictions across different pollution backgrounds. In KJ, the performance gap between predictions and GEMS is minimized, with very close RMSE (approx. 1.87–1.93 vs. 1.72–1.91 Pmolec/cm^2) and MAE values. In NI, the predictions also show excellent reliability: in 2023, its RMSE (1.799 Pmolec/cm^2) and MAE (1.179 Pmolec/cm^2) were both lower than those of GEMS for the same period (RMSE = 2.076 Pmolec/cm^2, MAE = 1.352 Pmolec/cm^2).

Overall, the independent validation based on GOME-2C demonstrates that the predictions from PhysNorm-Net can stably maintain a high overall correlation and a relatively controlled level of error during the 2019–2024 period. Furthermore, it did not show significant performance degradation in the retrospective years without GEMS label support. This indicates that the reconstructed dataset not only effectively inherits the spatiotemporal distribution information from GEMS but also has the potential for extension to historical periods, providing a reliable foundation for constructing long-term, hourly tropospheric NO_2 datasets.

4.3 Spatiotemporal analysis of the dataset predicted by PhysNorm-Net

Leveraging the predicted hourly tropospheric NO_2 dataset from 2019 to 2024, this section systematically analyzes the spatiotemporal features of tropospheric NO_2 across the four study regions, focusing on diurnal variations and inter-annual evolution at different spatial scales.

Figure 7 presents the multi-year average Month-Hour 2D heatmaps of NO_2 for the four regions. In the East Asian regions (NP, CC, KJ), an NO_2 valley typically appears between 12:00–14:00 local time (LT), with high-value bands in the morning (around 08:00 LT) and evening (after 17:00 LT). Seasonally, they always exhibit high values in winter and low values in summer. This macroscopic feature aligns well with physical expectations: the bimodal morning and evening peaks are primarily attributed to concentrated emissions from rush-hour traffic coupled with a shallower planetary boundary layer, while the midday trough is due to strong photochemical dissociation of NO_2 induced by intense solar radiation. The NI region exhibits a seasonal phase distinct from that of East Asia, with its highest concentrations occurring not in winter but in the spring (March–May, the pre-monsoon period). This unique characteristic may reflect a combination of intense surface heating, frequent agricultural biomass burning, and potentially weakened photochemical loss due to aerosol-radiation feedback from heavy dust aerosols, collectively leading to extremely high NO_2 loads. This evolution of diurnal patterns with the seasons highlights the necessity of high-frequency and high-coverage observations for capturing complex regional pollution mechanisms.

https://doi.org/10.5194/essd-2026-443
Preprint. Discussion started: 24 June 2026

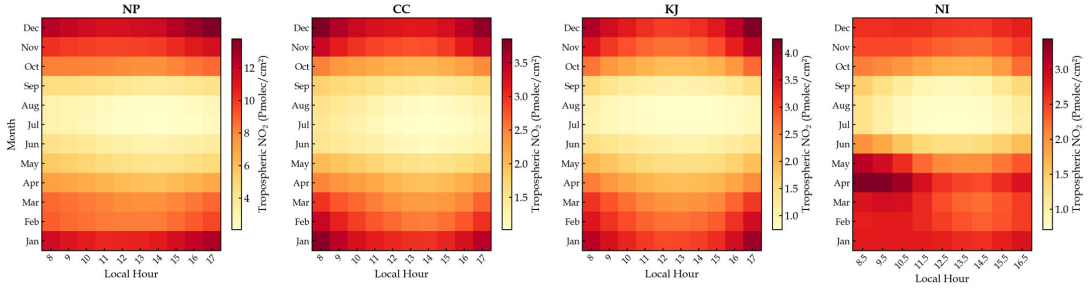

Figure 7: Month-Hour 2D distribution of tropospheric NO_2 in the four study regions from 2019 to 2024.

Beyond the regional macroscopic patterns, Figure 8 focuses on four representative cities (Beijing, Chengdu, Seoul, and Delhi) to reveal the fine-grained diurnal structures and their inter-annual evolution under the coupled influence of local emissions and meteorological conditions. The diurnal amplitude in Beijing is higher in winter (DJF), while in summer (JJA), strong photolysis suppresses the overall background values and weakens the amplitude. From 2019 to 2024, the diurnal curves for all seasons in Beijing show a parallel downward shift, indicating that regional emission reduction policies have had a systematic, all-day effect. Chengdu's diurnal variation is relatively flat, directly reflecting the topographic enclosure effect of the Sichuan Basin, where surrounding mountains block horizontal ventilation and persistent inversion layers limit boundary layer development, causing daytime photolysis consumption of NO_2 to be partially offset by limited dispersion conditions. The smaller decrease in Chengdu's six-year average is consistent with the relatively slower industrial restructuring in the basin; the brief rebound in 2021 may be related to post-pandemic industrial recovery. Seoul exhibits an afternoon peak in winter and spring, suggesting that its NO_2 load is not solely driven by local morning rush-hour traffic but is strongly influenced by regional transport from surrounding industrial areas. Seoul's decrease over the six years is the largest among the four cities, confirming the effectiveness of South Korea's recent coal-fired power plant phase-out policies. Delhi is strongly modulated by the South Asian monsoon system. Its diurnal amplitude is largest in the pre-monsoon spring, with extremely high morning values followed by a sharp afternoon drop. During the summer monsoon (JJA), all-day concentrations plummet to their annual minimum due to efficient wet scavenging and convective mixing from monsoon precipitation.

https://doi.org/10.5194/essd-2026-443
Preprint. Discussion started: 24 June 2026

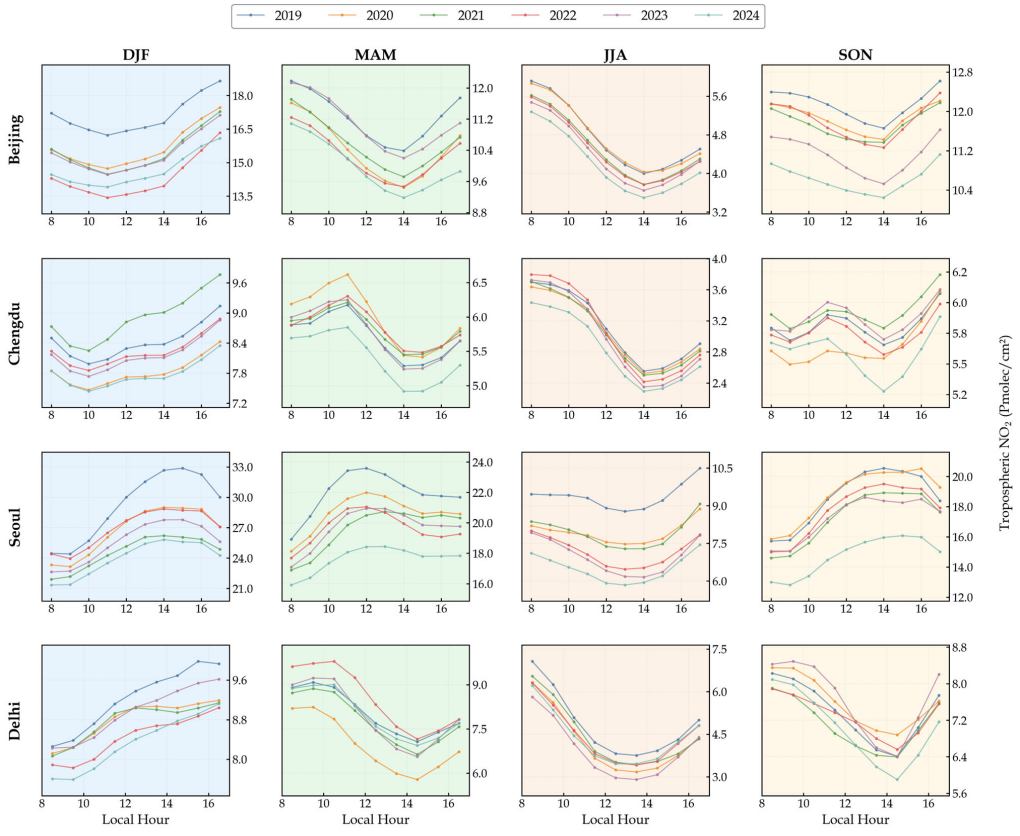

Figure 8: Inter-annual evolution of seasonal diurnal variations of tropospheric NO_2 in Beijing, Chengdu, Seoul, and Delhi from 2019 to 2024.

Figures 9 and 10 decompose the annual regional mean values by time of day (All-day: 8–17 LT, Morning: 8–10 LT, Noon: 11–13 LT, Afternoon: 14–17 LT) to assess inter-annual differences both temporally and spatially. In the NP region, Figure 9 shows a highly consistent decreasing trend. Figure 10 (2019–2024 panel) spatially pinpoints the core areas of emission reduction: the densely populated and industrialized zone centered on the Beijing-Tianjin-Hebei region to the Shandong Peninsula experienced a drastic decrease of over 10%. The more significant drop from 2023 to 2024 compared to previous years strongly validates the effectiveness of the region's environmental management policies. Temporally, the decrease in the morning was slightly larger than at noon and in the afternoon from 2019 to 2020, likely due to the reduced morning rush-hour effect from decreased commuting during the pandemic.

The CC region experienced a rebound in 2021 after a decrease in 2020, exhibiting a post-pandemic economic recovery feature. Spatially, from 2019 to 2024, the three core cities of Chengdu, Chongqing, and Xi'an show patchy decreases, but some surrounding industrial nodes still exhibit local concentration increases, possibly reflecting complex industrial structural shifts. Compared with the phenomenon that the overall decline of NP was relatively consistent across the three time periods, the decline of CC was the highest in the afternoon during the period from 2019 to 2024.

https://doi.org/10.5194/essd-2026-443
Preprint. Discussion started: 24 June 2026

595 The KJ region, amidst an overall downward trend, also experienced localized rebounds, such as in 2022 mainly over South
596 Korea and nearby waters, and near Incheon in 2021. Despite these short-term fluctuations, the overall trend from 2019 to 2024
597 shows that emission reduction efforts in the Korea-Japan region have been highly effective, with nearly all valid pixels showing
598 varying degrees of concentration decrease. This pattern of widespread emission reduction in these areas, with particularly
599 significant effects in major cities, is highly consistent with NP.

600 In contrast, the change of NO_2 distribution in the NI region is more complex, displaying a spatially heterogeneous pattern.
601 The Indo-Gangetic Plain shows a complex mosaic of increases and decreases along the northwest-to-southeast economic corridor.
602 Notably, in 2022, large areas in the middle and lower reaches of the plain experienced increases, possibly linked to the expansion
603 of energy-intensive industries under post-pandemic economic stimulus. The overall comparison between 2024 and 2019 indicates
604 that while individual large cities (like Delhi) show sporadic decreases, the vast mixed agricultural and emerging industrial zones
605 are still in a phase of increasing concentrations, highlighting the severe air quality management pressure the region continues to
606 face.

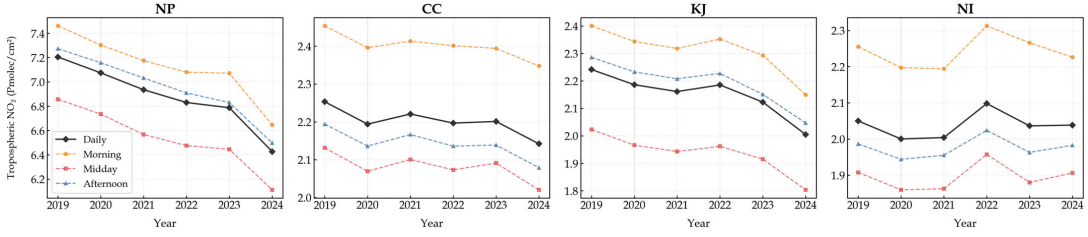

607

608 **Figure 9: Inter-annual variation of tropospheric NO_2 in the four study regions during All-day, Morning, Noon, and**
609 **Afternoon periods from 2019 to 2024.**

https://doi.org/10.5194/essd-2026-443
Preprint. Discussion started: 24 June 2026

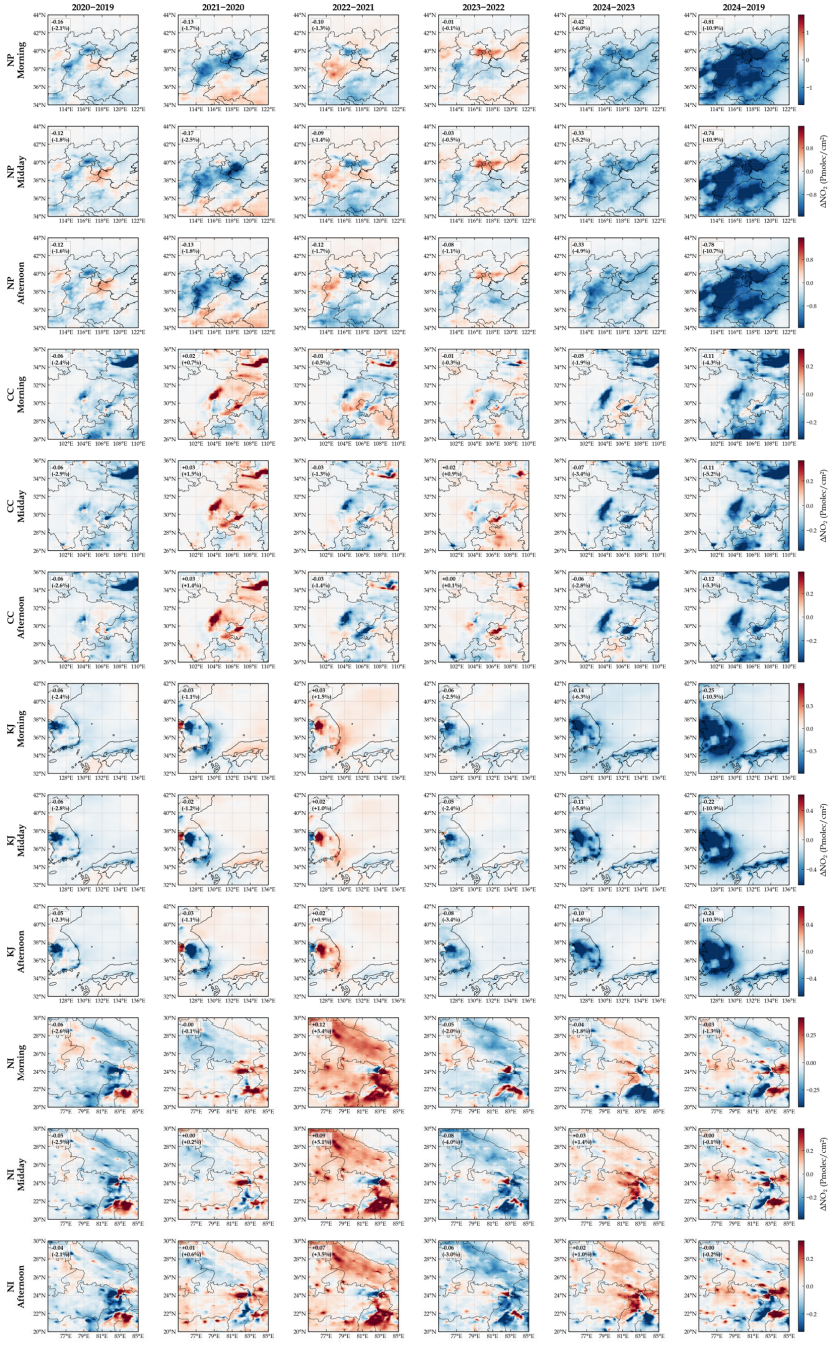

610

611 **Figure 10: Spatial distribution of inter-annual differences in tropospheric NO_2 for different time slots in the four study**
612 **regions from 2019 to 2024.**

https://doi.org/10.5194/essd-2026-443
Preprint. Discussion started: 24 June 2026

5. Discussion

5.1 Physical interpretability and feature importance analysis of PhysNorm-Net

The following diagnostics are reported to build trust in the dataset by demonstrating that the reconstruction responds to physical drivers, rather than as a stand-alone mechanistic study. This study first verified the functional integrity and physical responsiveness of the dual-branch architecture through a model diagnostic experiment (Fig. 11). The experiment compared the outputs of the normal prediction mode (using both satellite observations and physical prior inputs) with a "blind test" mode (where satellite branch inputs were zeroed out with a full missing-data mask, forcing the model to rely solely on the physical branch). This was done to examine the model's sensitivity to changes in physical inputs. The diagnostic results show that the model can still output the general distribution of NO_2 even when relying exclusively on the physical branch, which ensures predictive capability during periods without TROPOMI observations. The inclusion of the satellite branch then effectively corrects the concentration details and gradients. From a functional validation perspective, this finding confirms that the physical branch plays a primary role in providing foundational information, while the satellite branch is mainly responsible for the fine-grained refinement of high-resolution details.

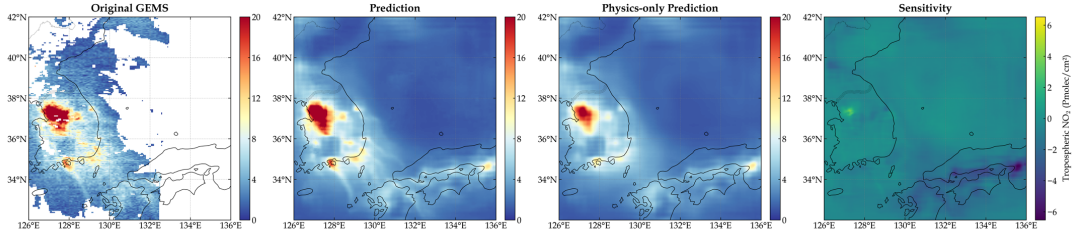

Figure 11: Functional diagnostic experiment of the PhysNorm-Net dual-branch architecture.

Building on this diagnostic foundation, to further unveil the model's decision-making mechanism, we quantitatively analyzed the relative contributions of each input variable during daytime hours in 2023 using a zero-out perturbation method (Zhang and Gao, 2020). This method calculates a variable's importance score by zeroing out its specific channel and measuring the resulting deviation from the baseline output, quantified by MAE. Figure 12 presents the top three variables for each region, month, and hour. The dominant variable combinations differ significantly across the four regions, indicating that the model does not simply rely on a fixed set of factors but instead forms region-specific control structures. In Figure 13, variables are categorized into seven physical groups: thermodynamics (specific humidity and temperature), dynamic transport (surface pressure and u/v component of wind), static geography (DEM and land use), chemical prior (EAC4), radiation (SZA), boundary layer & cloud (boundary layer height and total cloud cover), and satellite observation (TROPOMI), quantitatively presenting the diurnal variation of their grouped importance. The common feature shared by all regions is that thermodynamics, dynamic transport and static geography are usually the top three categories, while SZA shows periodic changes throughout the day.

https://doi.org/10.5194/essd-2026-443
Preprint. Discussion started: 24 June 2026

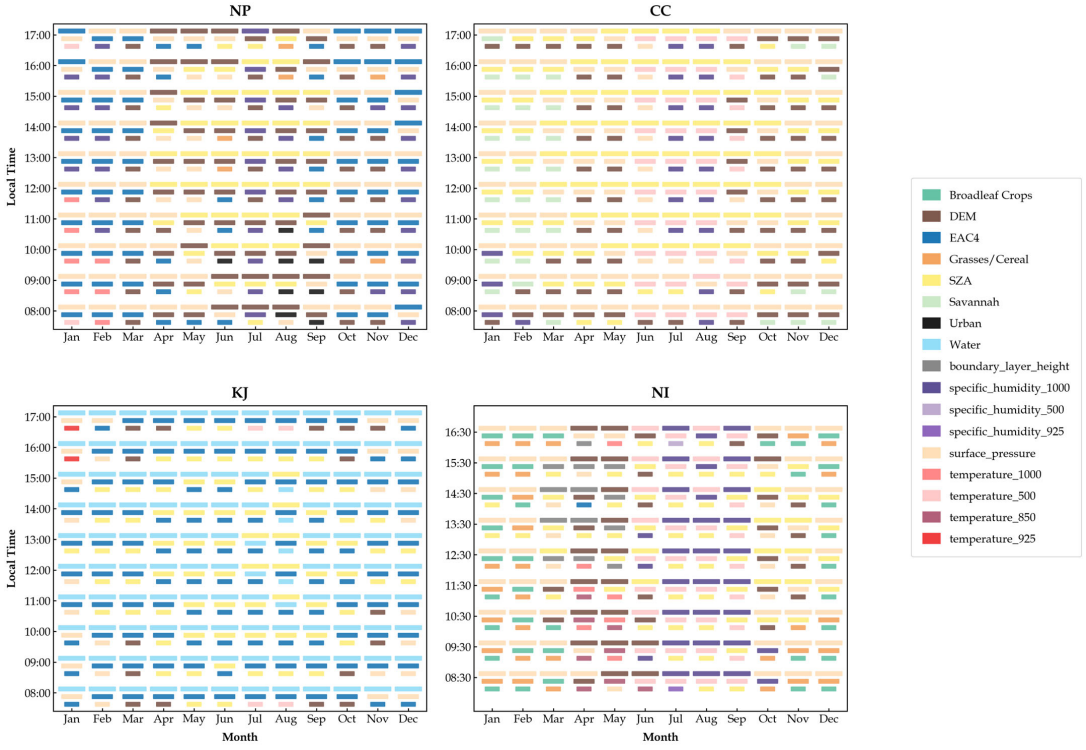

Figure 12: Monthly and hourly feature importance rankings for the four regions based on the zero-out perturbation method.

https://doi.org/10.5194/essd-2026-443
Preprint. Discussion started: 24 June 2026

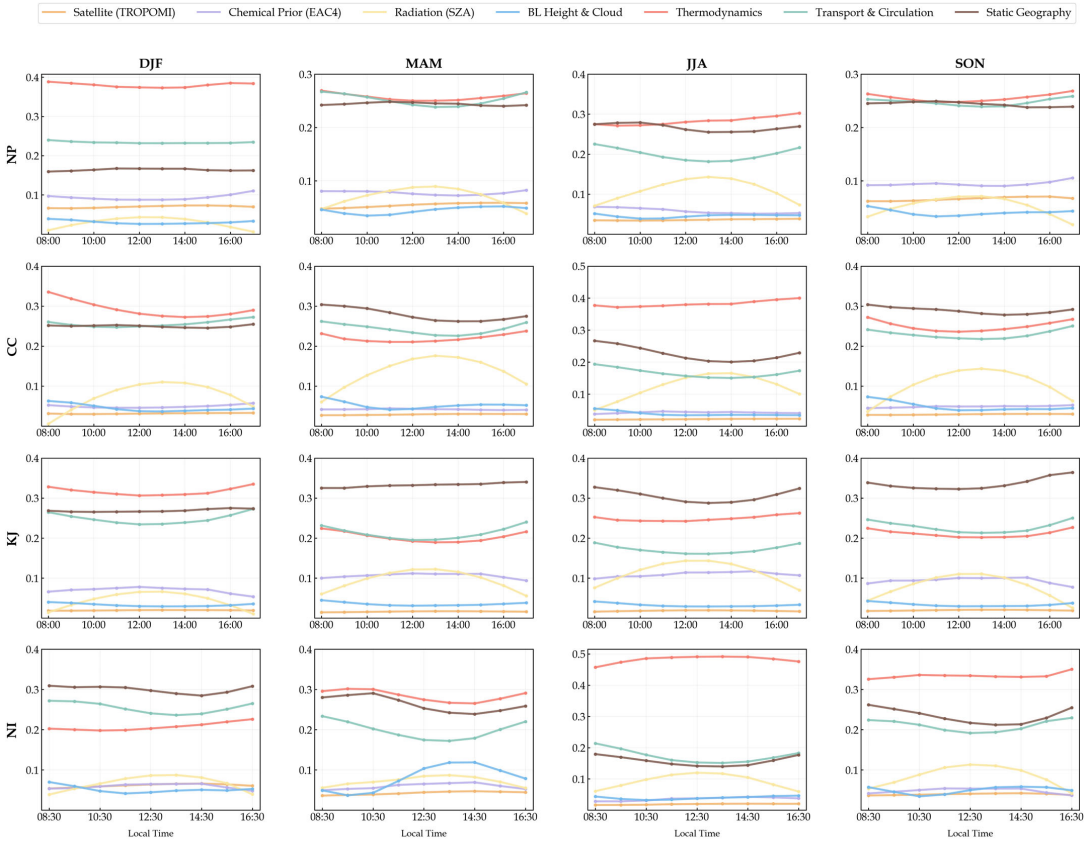

Figure 13: Diurnal variation of grouped feature importance.

Combining Figs. 12 and 13, in the NP region, the most stable and prominent variables during winter and late autumn are EAC4 and surface pressure, with the third position often supplemented by a near-surface or mid-tropospheric thermodynamic variables. However, thermodynamic variables take the lead (~0.37–0.38) after grouping. This arrangement has a clear physical meaning: in East Asian winters, frequent temperature inversions, stable weather conditions, and high relative humidity collectively suppress vertical mixing and promote the accumulation of NO_2 in the near-surface layer (Chai et al., 2014; Xu et al., 2011). Concurrently, at certain times during winter, poor GEMS observation conditions reduce the number of training labels, causing the model to learn more from the total column concentration information provided by EAC4. In summer (JJA), the contributions of the thermodynamics and transport groups decline (to ~0.27–0.30 and ~0.18–0.22, respectively), while SZA significantly increases, and shows a strong daytime peak at noon. This aligns with the physical processes of enhanced convective mixing and accelerated photochemical decomposition in the warm season (Liu et al., 2022).

In the CC region, surface pressure ranks first during most daytime hours throughout the year, and the corresponding group consistently occupies the top three throughout the year. This result is highly consistent with the fundamental understanding of air pollution distribution in a basin: within an enclosed topography, surface pressure not only reflects the state of synoptic-scale circulation but also indirectly indicates ventilation capacity and pollution trapping conditions (Sun et al., 2020). Static geographical

https://doi.org/10.5194/essd-2026-443
Preprint. Discussion started: 24 June 2026

variables also occupy the top three throughout the year, indicating that local terrain height differences and land cover types play a persistent role in shaping the spatial pattern of NO_2, providing a stable spatial constraint framework for the model. After entering summer, the contribution of the thermodynamic group rises to nearly 0.4, and the role of independent variables begins to become prominent. At the same time, the importance of SZA also increases in spring and summer, and it becomes the variable with the highest contribution. This is consistent with the meteorological background of the Sichuan Basin in summer, which is characterized by the development of thermal lows, valley winds, and enhanced convective mixing (Feng et al., 2022).

In the KJ region, water body is the top-ranked variable in almost all months and daytime hours, and in the group results, static geography also ranks first in three seasons. This implies that in a peninsula-archipelago system with complex coastlines and strong land-sea segmentation, the water body variable effectively encodes the regional land-sea distribution, which in turn determines the spatial extent of emission sources and sea breeze influence. Furthermore, the contribution of the thermodynamics group (~0.30–0.35) is significantly higher in DJF. And the importance of EAC4 becomes more pronounced in the cold season and in the early and late periods when it is treated as an independent variable. This variation shows that the spatial pattern in the KJ region is first fixed by the land-sea distribution, after which its explanatory power is enhanced by the continental background and stable stratification in the cold season, whereas it is modulated more by solar radiation and thermodynamic conditions in the warm season.

The NI region exhibits a strong seasonal switch. During winter and late autumn, surface pressure is almost consistently ranked first, indicating that NO_2 distribution in this region is primarily controlled by boundary layer stability and ventilation conditions during the cold and transitional seasons. Concurrently, the land use types grasslands/cereal crops and broadleaf crops become prominent in winter. These agricultural land types are widespread in the Indo-Gangetic Plain, and their high importance reflects the impact of agricultural burning—the widespread burning of crop residues in this region is a major seasonal source of NO_x (Cusworth et al., 2018; Jethva et al., 2018). Around the monsoon season, the dominant variables shift to specific humidity, temperature, and SZA, and the contribution of thermodynamics rises to nearly 0.5, while the importance of land use variables significantly decreases. This reflects the profound influence of monsoon dynamics on vertical mixing, wet scavenging, and the large-scale redistribution of pollutants (Ravindra et al., 2003).

It is important to note that TROPOMI's importance score is generally lower than the sum of the physical variable groups. This is partly due to its spatiotemporal incompleteness and partly due to differences in information density compared to the physical variable groups. Additionally, the zero-out perturbation method tests the model's dependency on an input, not its strict physical causal contribution. Therefore, the importance of static variables like land use and DEM should be understood as the model's reliance on spatial encoding and regional templates.

5.2 Limitations and future work

Although the reconstructed dataset demonstrates high accuracy in independent validations, users should note certain inherent limitations when utilizing these data.

First, regarding the spatial sampling strategy for the training domain, this study prioritized representative high-emission and complex-terrain regions. This approach enabled the model to be guided to learn key physical processes such as emission accumulation, boundary layer constraints, and regional transport. This effectively mitigates the risks of global gradient dilution and systematic underestimation that can arise from the long-tail distribution of global tropospheric NO_2 (i.e., vast areas of clean atmosphere and low-value ocean regions). However, this non-uniform sampling strategy objectively limits the model's generalizability to extremely low-concentration backgrounds, such as those found in clean tropical atmospheres. Consequently, while the dataset excels in capturing hotspots, it may possess higher relative uncertainties in extremely clean, low-concentration atmospheric backgrounds (e.g., remote oceanic regions). Users focusing on ultra-low background concentrations should apply

https://doi.org/10.5194/essd-2026-443
Preprint. Discussion started: 24 June 2026

these data with caution. Future work will focus on developing adaptive global sampling strategies and dynamic loss function weighting mechanisms to achieve a better fitting balance between extremely polluted hotspots and ultra-low background concentrations. Furthermore, the current framework is primarily trained on data from a single year; incorporating a longer time series into the training set would significantly enhance the model's robustness to extreme meteorological anomalies and inter-annual baseline shifts in emissions.

Second, in addition to the existing four key hotspots datasets, users can also apply this model to other regions. Since the physicochemical evolution of tropospheric NO_2 is highly dependent on local environments, pretrained models objectively face domain shift challenges in direct cross-regional applications. Experiments show that instead of retraining the entire network, the model can be rapidly adapted by performing lightweight fine-tuning on the core PhysNorm layers using only a small, stratified sample of data from the target region. For example, in the Yangtze River Delta region, which shares similar characteristics with the source training domains, direct transfer yields a reasonable accuracy of $R^2 = 0.74$, which improves to 0.87 after fine-tuning. This demonstrates that through efficient parameter updates, the physics-guided module can quickly realign with the new regional meteorological and chemical prior fields. Naturally, greater caution should be exercised when extending the model to regions with vastly different emission patterns; in such cases, retraining the framework for the target region might be a more prudent choice.

Finally, at the data product level, integrating the 0.25° physical prior fields with the 0.05° high-resolution observations introduces a minor spatial smoothing effect. The smoothing effect is an intended and reasonable constraint imposed by the physical fields on the noise inherent in remote sensing retrievals. However, users investigating highly localized, single-point extreme emission sources should account for this slight gradient smoothing in their analyses. It is also noted that all input images underwent rigorous normalization pre-processing before being fed into the network, which synergizes well with the internal feature normalization to ensure training stability. With the successive launches of new-generation geostationary environmental satellites like TEMPO and Sentinel-4, it is envisioned that this framework proposed in this study could be used to achieve a broader and more extensive production of datasets. By properly addressing inter-sensor systematic biases, this would enable seamless, hourly, and quasi-global mapping of NO_2 dynamics.

6. Conclusions

This study presents the first seamless, 0.05° hourly tropospheric NO_2 vertical column density dataset covering typical Asian hotspots from 2019 to 2024. To overcome the core challenges of spatial discontinuity and short historical records inherent in high-frequency geostationary satellite data, this dataset was reconstructed using an advanced physics-aware deep learning framework (PhysNorm-Net).

The high quality and physical reliability of this dataset are ensured through a rigorous multi-modal fusion mechanism. First, this study utilizes a Partial Convolutional network with dynamic mask updates to effectively isolate mean-value contamination from invalid pixels, enabling the precise extraction of high-resolution spatial textures. Second, deviating from traditional channel-wise concatenation, PhysNorm module uses multi-level meteorological, topographical, and chemical prior fields as environmental context to adaptively control the affine transformation of high-resolution features. This ensures that the reconstructed concentration fields strictly adhere to the physical laws of advection-diffusion and photochemical reactions. Third, the loss function adopts a combination of fine-grained reconstruction and coarse-grained physical consistency constraints to further mitigate the gradient dilution problem in deep networks.

Quantitative assessments confirm that the reconstructed dataset achieves extremely high fitting accuracy on the test set ($R^2 = 0.889$) and can effectively recover morning and evening pollution hotspots missed by polar-orbiting instruments like TROPOMI

https://doi.org/10.5194/essd-2026-443
Preprint. Discussion started: 24 June 2026

due to their spatiotemporal coverage limitations. More importantly, the long-term retrospective validation against GOME-2C data (R = 0.780) not used in the PhysNorm-Net training demonstrates that the dataset possesses robust temporal stability and high fidelity in historical periods (2019–2022) prior to the operational deployment of GEMS.

Through in-depth analysis, this newly generated long-term hourly dataset has proven its unique scientific utility in capturing complex atmospheric dynamics. It not only clearly reveals the monsoon-driven seasonal phase reversal in North India and the typical bimodal and single-trough diurnal pattern in East Asia, but also effectively quantifies the significant effects of continuous emission reduction policies in the North China Plain and the Korea-Japan region since 2019, as well as localized pollution rebounds due to economic recovery in specific years (e.g., 2021). By bridging the gap between sparse retrievals and continuous physical priors, this dataset provides an unprecedented and essential infrastructural foundation for tracking long-term air pollution trends, conducting health exposure assessments, and supporting epidemiological research across Asia.

Data availability

TROPOMI (https://doi.org/10.5270/S5P-9bnp8q8) and MCD12C1 (https://doi.org/10.5067/MODIS/MCD12C1.061) data used in this study are available on the EARTHDATA platform. GEMS data can be accessed at https://nesc.nier.go.kr/en/html/datasvc/data.do?pageIndex=1&outputInnb=64&atrb=NO2_Trop. The GOME-2 data are provided by the EUMETSAT AC-SAF as described in https://acsaf.org/products/nto_no2.php. ERA5 on single and pressure levels can be accessed at https://cds.climate.copernicus.eu/datasets/reanalysis-era5-single-levels?tab=overview and https://cds.climate.copernicus.eu/datasets/reanalysis-era5-pressure-levels?tab=overview, respectively. EAC4 data can be accessed at https://ads.atmosphere.copernicus.eu/datasets/cams-global-reanalysis-eac4?tab=overview. ETOPO data can be found at https://www.ncei.noaa.gov/products/etopo-global-relief-model. The gapless 0.05° hourly tropospheric NO_2 dataset (2019–2024) produced in this study is available at https://doi.org/10.5281/zenodo.20427767 (Gao et al., 2026).

Author contributions

Hongrui Gao: Methodology, Investigation, Formal Analysis, Visualization, Data Curation, Writing – Original Draft; Qin He: Conceptualization, Investigation, Writing – Review & Editing. Kai Qin: Funding Acquisition, Project Administration, Supervision. Jhoon Kim: Writing – Review & Editing. Diego Loyola: Writing – Review & Editing. Pravash Tiwari: Writing – Review & Editing. Lingxiao Lu: Writing – Review & Editing. Jason B. Cohen: Supervision, Writing – Review & Editing.

Competing interests

The authors declare that they have no conflict of interest.

Financial support

This work was supported by the National Natural Science Foundation of China [Grant Numbers 42375125].

https://doi.org/10.5194/essd-2026-443
Preprint. Discussion started: 24 June 2026

765 **References**

766 Ahmad, N., Lin, C., Lau, A. K. H., Kim, J., Zhang, T., Yu, F., Li, C., Li, Y., Fung, J. C. H., and Lao, X. Q.: Estimation of ground-
767 level NO_2 and its spatiotemporal variations in China using GEMS measurements and a nested machine learning model,
768 Atmospheric Chemistry and Physics, 24, 9645–9665, https://doi.org/10.5194/acp-24-9645-2024, 2024.
769 Alvera-Azcárate, A., Barth, A., Rixen, M., and Beckers, J. M.: Reconstruction of incomplete oceanographic data sets using
770 empirical orthogonal functions: application to the Adriatic Sea surface temperature, Ocean Modell., 9, 325–346,
771 https://doi.org/10.1016/j.ocemod.2004.08.001, 2005.
772 Auer, A. H.: Correlation of Land Use and Cover with Meteorological Anomalies, Journal of Applied Meteorology (1962-1982),
773 17, 636–643, https://doi.org/10.1175/1520-0450(1978)017%3C0636:COLUAC%3E2.0.CO;2, 1978.
774 Baruah, U. D., Robeson, S. M., Saikia, A., Mili, N., Sung, K., and Chand, P.: Spatio-temporal characterization of tropospheric
775 ozone and its precursor pollutants NO2 and HCHO over South Asia, Science of The Total Environment, 809, 151135,
776 https://doi.org/10.1016/j.scitotenv.2021.151135, 2022.
777 Beelen, R., Hoek, G., Vienneau, D., Eeftens, M., Dimakopoulou, K., Pedeli, X., Tsai, M.-Y., Künzli, N., Schikowski, T., Marcon,
778 A., Eriksen, K. T., Raaschou-Nielsen, O., Stephanou, E., Patelarou, E., Lanki, T., Yli-Tuomi, T., Declercq, C., Falq, G., Stempfelet,
779 M., Birk, M., Cyrys, J., Von Klot, S., Nádor, G., Varró, M. J., Dėdelė, A., Gražulevičienė, R., Mölter, A., Lindley, S., Madsen, C.,
780 Cesaroni, G., Ranzi, A., Badaloni, C., Hoffmann, B., Nonnemacher, M., Krämer, U., Kuhlbusch, T., Cirach, M., De Nazelle, A.,
781 Nieuwenhuijsen, M., Bellander, T., Korek, M., Olsson, D., Strömgren, M., Dons, E., Jerrett, M., Fischer, P., Wang, M., Brunekreef,
782 B., and De Hoogh, K.: Development of NO2 and NOx land use regression models for estimating air pollution exposure in 36 study
783 areas in Europe – The ESCAPE project, Atmos. Environ., 72, 10–23, https://doi.org/10.1016/j.atmosenv.2013.02.037, 2013.
784 Beirle, S., Boersma, K. F., Platt, U., Lawrence, M. G., and Wagner, T.: Megacity Emissions and Lifetimes of Nitrogen Oxides
785 Probed from Space, Science, 333, 1737–1739, https://doi.org/10.1126/science.1207824, 2011.
786 Boersma, K. F., Eskes, H. J., Veefkind, J. P., Brinksma, E. J., van der A, R. J., Sneep, M., van den Oord, G. H. J., Levelt, P. F.,
787 Stammes, P., Gleason, J. F., and Bucsela, E. J.: Near-real time retrieval of tropospheric NO_2 from OMI, Atmospheric Chemistry
788 and Physics, 7, 2103–2118, https://doi.org/10.5194/acp-7-2103-2007, 2007.
789 Boersma, K. F., Eskes, H. J., Dirksen, R. J., van der A, R. J., Veefkind, J. P., Stammes, P., Huijnen, V., Kleipool, Q. L., Sneep,
790 M., Claas, J., Leitão, J., Richter, A., Zhou, Y., and Brunner, D.: An improved tropospheric NO_2 column retrieval algorithm for the
791 ozone monitoring instrument, Atmospheric Measurement Techniques, 4, 1905–1928, https://doi.org/10.5194/amt-4-1905-2011,
792 2011a.
793 Boersma, K. F., Eskes, H. J., Dirksen, R. J., van der A, R. J., Veefkind, J. P., Stammes, P., Huijnen, V., Kleipool, Q. L., Sneep,
794 M., Claas, J., Leitão, J., Richter, A., Zhou, Y., and Brunner, D.: An improved tropospheric NO2 column retrieval algorithm for the
795 ozone monitoring instrument, Atmospheric Measurement Techniques, 4, 1905–1928, https://doi.org/10.5194/amt-4-1905-2011,
796 2011b.
797 Bovensmann, H., Burrows, J. P., Buchwitz, M., Frerick, J., Noël, S., Rozanov, V. V., Chance, K. V., and Goede, A. P. H.:
798 SCIAMACHY: Mission objectives and measurement modes, 1999.
799 Burnett, R. T., Stieb, D., Brook, J. R., Cakmak, S., Dales, R., Raizenne, M., Vincent, R., and Dann, T.: Associations between
800 Short-Term Changes in Nitrogen Dioxide and Mortality in Canadian Cities, Archives of Environmental Health: An International
801 Journal, 59, 228–236, https://doi.org/10.3200/AEOH.59.5.228-236, 2004.

https://doi.org/10.5194/essd-2026-443
Preprint. Discussion started: 24 June 2026

802 Burrows, J. P., Weber, M., Buchwitz, M., Rozanov, V., Ladstätter-Weißenmayer, A., Richter, A., DeBeek, R., Hoogen, R.,
803 Bramstedt, K., Eichmann, K.-U., Eisinger, M., and Perner, D.: The global ozone monitoring experiment (GOME): Mission concept
804 and first scientific results, 1999.
805 Callies, J., Corpaccioli, E., Eisinger, M., Hahne, A., and Lefebvre, A.: GOME-2-metop's second-generation sensor for operational
806 ozone monitoring, ESA Bull., 102, 28–36, 2000.
807 Chai, F., Gao, J., Chen, Z., Wang, S., Zhang, Y., Zhang, J., Zhang, H., Yun, Y., and Ren, C.: Spatial and temporal variation of
808 particulate matter and gaseous pollutants in 26 cities in China, Journal of Environmental Sciences, 26, 75–82,
809 https://doi.org/10.1016/S1001-0742(13)60383-6, 2014.
810 Chan, K. L., Valks, P., Heue, K.-P., Lutz, R., Hedelt, P., Loyola, D., Pinardi, G., Van Roozendael, M., Hendrick, F., Wagner, T.,
811 Kumar, V., Bais, A., Piters, A., Irie, H., Takashima, H., Kanaya, Y., Choi, Y., Park, K., Chong, J., Cede, A., Frieß, U., Richter, A.,
812 Ma, J., Benavent, N., Holla, R., Postylyakov, O., Rivera Cárdenas, C., and Wenig, M.: Global ozone monitoring experiment-2
813 (GOME-2) daily and monthly level-3 products of atmospheric trace gas columns, Earth System Science Data, 15, 1831–1870,
814 https://doi.org/10.5194/essd-15-1831-2023, 2023.
815 Chang, B., Liu, H., Zhang, C., Xing, C., Tan, W., and Liu, C.: Relating satellite NO2 tropospheric columns to near-surface
816 concentrations: implications from ground-based MAX-DOAS NO2 vertical profile observations, Npj Clim. Atmos. Sci., 8, 1,
817 https://doi.org/10.1038/s41612-024-00891-z, 2025.
818 Chen, T.-H., Hsu, Y.-C., Zeng, Y.-T., Candice Lung, S.-C., Su, H.-J., Chao, H. J., and Wu, C.-D.: A hybrid kriging/land-use
819 regression model with asian culture-specific sources to assess NO2 spatial-temporal variations, Environmental Pollution, 259,
820 113875, https://doi.org/10.1016/j.envpol.2019.113875, 2020.
821 Choi, H., Liu, X., Jeong, U., Chong, H., Kim, J., Ahn, M. H., Ko, D. H., Lee, D.-W., Moon, K.-J., and Lee, K.-M.: Geostationary
822 environment monitoring spectrometer (GEMS) polarization characteristics and correction algorithm, Atmospheric Measurement
823 Techniques, 17, 145–164, https://doi.org/10.5194/amt-17-145-2024, 2024.
824 Cusworth, D. H., Mickley, L. J., Sulprizio, M. P., Liu, T., Marlier, M. E., DeFries, R. S., Guttikunda, S. K., and Gupta, P.:
825 Quantifying the influence of agricultural fires in northwest India on urban air pollution in Delhi, India, Environ. Res. Lett., 13,
826 044018, https://doi.org/10.1088/1748-9326/aab303, 2018.
827 Duncan, B. N., Lamsal, L. N., Thompson, A. M., Yoshida, Y., Lu, Z., Streets, D. G., Hurwitz, M. M., and Pickering, K. E.: A
828 space-based, high-resolution view of notable changes in urban NOx pollution around the world (2005–2014), Journal of
829 Geophysical Research: Atmospheres, 121, 976–996, https://doi.org/10.1002/2015JD024121, 2016.
830 von Engeln, A. and Teixeira, J.: A planetary boundary layer height climatology derived from ECMWF reanalysis data, Journal of
831 Climate, 26, 6575–6590, https://doi.org/10.1175/JCLI-D-12-00385.1, 2013.
832 Fan, Y., Sun, L., and Liu, X.: GOCI-II geostationary satellite hourly aerosol optical depth obtained by data-driven methods:
833 Validation and comparison, Atmos. Environ., 310, 119965, https://doi.org/10.1016/j.atmosenv.2023.119965, 2023.
834 Feng, X., Wang, S., and Guo, J.: Temperature inversions in the lower troposphere over the sichuan basin, China: Seasonal feature
835 and relation with regional atmospheric circulations, Atmospheric Research, 271, 106097,
836 https://doi.org/10.1016/j.atmosres.2022.106097, 2022.
837 Flemming, J., Peuch, V. H., and Jones, L.: Ten years of forecasting atmospheric composition at ECMWF, in: ECMWF Newsletter,
838 vol. 152, 2017.
839 Friedl, M. and Sulla-Menashe, D.: MODIS/Terra+ Aqua land cover type yearly L3 global 0.05 Deg CMG V061, NASA EOSDIS
840 Land Processes Distributed Active Archive Center (DAAC) data set, MCD12C1. 061, 2022.

https://doi.org/10.5194/essd-2026-443
Preprint. Discussion started: 24 June 2026

841 Fu, J., Tang, D., Grieneisen, M. L., Yang, F., Yang, J., Wu, G., Wang, C., and Zhan, Y.: A machine learning-based approach for
842 fusing measurements from standard sites, low-cost sensors, and satellite retrievals: Application to NO2 pollution hotspot
843 identification, Atmos. Environ., 302, 119756, https://doi.org/10.1016/j.atmosenv.2023.119756, 2023.
844 Gao, H., He, Q., Qin, K., Kim, J., Tiwari, P., Lu, L., and Cohen, J. B.: A gapless 0.05° hourly tropospheric NO2 dataset (2019–
845 2024) over key Asian hotspots reconstructed using physics-aware deep learning, https://doi.org/10.5281/zenodo.20427767, 2026.
846 Geffen, V., Eskes, H., Boersma, K., Maasakkers, J., and Veefkind, J.: TROPOMI ATBD of the total and tropospheric NO2 data
847 products, DLR document, 2019.
848 Gohm, A., Harnisch, F., Vergeiner, J., Obleitner, F., Schnitzhofer, R., Hansel, A., Fix, A., Neininger, B., Emeis, S., and Schäfer,
849 K.: Air pollution transport in an alpine valley: Results from airborne and ground-based observations, Boundary-Layer Meteorol,
850 131, 441–463, https://doi.org/10.1007/s10546-009-9371-9, 2009.
851 Goldberg, D. L., Lu, Z., Streets, D. G., De Foy, B., Griffin, D., McLinden, C. A., Lamsal, L. N., Krotkov, N. A., and Eskes, H.:
852 Enhanced Capabilities of TROPOMI NO_2 : Estimating NO_X from North American Cities and Power Plants, Environ. Sci. Technol.,
853 53, 12594–12601, https://doi.org/10.1021/acs.est.9b04488, 2019.
854 Griffin, D., Zhao, X., McLinden, C. A., Boersma, F., Bourassa, A., Dammers, E., Degenstein, D., Eskes, H., Fehr, L., Fioletov, V.,
855 Hayden, K., Kharol, S. K., Li, S.-M., Makar, P., Martin, R. V., Mihele, C., Mittermeier, R. L., Krotkov, N., Sneep, M., Lamsal, L.
856 N., Linden, M. ter, Geffen, J. van, Veefkind, P., and Wolde, M.: High-Resolution Mapping of Nitrogen Dioxide With TROPOMI:
857 First Results and Validation Over the Canadian Oil Sands, Geophysical Research Letters, 46, 1049–1060,
858 https://doi.org/10.1029/2018GL081095, 2019.
859 Gu, J., Liang, X., Song, S., Li, Y., Chen, L., Tao, J., and Tian, Y.: Harmonizing satellite and ground NO2 observations in China:
860 A multi-sensor framework for scenario-specific calibration, ISPRS Journal of Photogrammetry and Remote Sensing, 230, 486–
861 494, https://doi.org/10.1016/j.isprsjprs.2025.09.028, 2025.
862 Handschuh, J., Baier, F., Molina García, V., Friedl, P., and Loyola, D.: TROPOMI-Based PM2.5 Estimates and Their Evaluation
863 During a High-Pollution Event in Germany, Remote Sensing, 18, 562, https://doi.org/10.3390/rs18040562, 2026.
864 Hassinen, S., Balis, D., Bauer, H., Begoin, M., Delcloo, A., Eleftheratos, K., Gimeno Garcia, S., Granville, J., Grossi, M., Hao, N.,
865 Hedelt, P., Hendrick, F., Hess, M., Heue, K.-P., Hovila, J., Jønch-Sørensen, H., Kalakoski, N., Kauppi, A., Kiemle, S., Kins, L.,
866 Koukouli, M. E., Kujanpää, J., Lambert, J.-C., Lang, R., Lerot, C., Loyola, D., Pedergnana, M., Pinardi, G., Romahn, F., van
867 Roozendael, M., Lutz, R., De Smedt, I., Stammes, P., Steinbrecht, W., Tamminen, J., Theys, N., Tilstra, L. G., Tuinder, O. N. E.,
868 Valks, P., Zerefos, C., Zimmer, W., and Zyrichidou, I.: Overview of the O3M SAF GOME-2 operational atmospheric composition
869 and UV radiation data products and data availability, Atmospheric Measurement Techniques, 9, 383–407,
870 https://doi.org/10.5194/amt-9-383-2016, 2016.
871 He, K., Zhang, X., Ren, S., and Sun, J.: Deep residual learning for image recognition, https://doi.org/10.48550/arXiv.1512.03385,
872 10 December 2015.
873 He, Q., Qin, K., Cohen, J. B., Loyola, D., Li, D., Shi, J., and Xue, Y.: Spatially and temporally coherent reconstruction of
874 tropospheric NO_2 over China combining OMI and GOME-2B measurements, Environ. Res. Lett., 15, 125011,
875 https://doi.org/10.1088/1748-9326/abc7df, 2020.
876 He, Q., Qin, K., Cohen, J. B., Li, D., and Kim, J.: Quantifying uncertainty in ML-derived atmosphere remote sensing: Hourly
877 surface NO2 estimation with GEMS, Geophysical Research Letters, 51, e2024GL110468, https://doi.org/10.1029/2024GL110468,
878 2024a.

https://doi.org/10.5194/essd-2026-443
Preprint. Discussion started: 24 June 2026

879 He, Z., Fan, G., Li, X., Gong, F.-Y., Liang, M., Gao, L., and Zhou, M.: Spatio-temporal modeling of satellite-observed CO2
880 columns in China using deep learning, Int. J. Appl. Earth Obs. Geoinf., 129, 103859, https://doi.org/10.1016/j.jag.2024.103859,
881 2024b.
882 Hengl, T., Heuvelink, G. B. M., and Rossiter, D. G.: About regression-kriging: From equations to case studies, Comput. Geosci.,
883 33, 1301–1315, https://doi.org/10.1016/j.cageo.2007.05.001, 2007.
884 Hersbach, H., Bell, B., Berrisford, P., Hirahara, S., Horányi, A., Muñoz-Sabater, J., Nicolas, J., Peubey, C., Radu, R., and Schepers,
885 D.: The ERA5 global reanalysis, Quarterly journal of the royal meteorological society, 146, 1999–2049,
886 https://doi.org/10.1002/qj.3803, 2020.
887 Hoek, G., Beelen, R., De Hoogh, K., Vienneau, D., Gulliver, J., Fischer, P., and Briggs, D.: A review of land-use regression models
888 to assess spatial variation of outdoor air pollution, Atmos. Environ., 42, 7561–7578,
889 https://doi.org/10.1016/j.atmosenv.2008.05.057, 2008.
890 Ialongo, I., Virta, H., Eskes, H., Hovila, J., and Douros, J.: Comparison of TROPOMI/Sentinel-5 Precursor NO_2 observations with
891 ground-based measurements in Helsinki, Atmospheric Measurement Techniques, 13, 205–218, https://doi.org/10.5194/amt-13-
892 205-2020, 2020.
893 Ingmann, P., Veihelmann, B., Langen, J., Lamarre, D., Stark, H., and Courrèges-Lacoste, G. B.: Requirements for the GMES
894 atmosphere service and ESA's implementation concept: Sentinels-4/-5 and -5p, Remote Sensing of Environment, 120, 58–69,
895 https://doi.org/10.1016/j.rse.2012.01.023, 2012.
896 Inness, A., Ades, M., Agustí-Panareda, A., Barré, J., Benedictow, A., Blechschmidt, A.-M., Dominguez, J. J., Engelen, R., Eskes,
897 H., Flemming, J., Huijnen, V., Jones, L., Kipling, Z., Massart, S., Parrington, M., Peuch, V.-H., Razinger, M., Remy, S., Schulz,
898 M., and Suttie, M.: The CAMS reanalysis of atmospheric composition, Atmospheric Chemistry and Physics, 19, 3515–3556,
899 https://doi.org/10.5194/acp-19-3515-2019, 2019.
900 Jethva, H., Chand, D., Torres, O., Gupta, P., Lyapustin, A., and Patadia, F.: Agricultural Burning and Air Quality over Northern
901 India: A Synergistic Analysis using NASA's A-train Satellite Data and Ground Measurements, Aerosol Air Qual. Res., 18, 1756–
902 1773, https://doi.org/10.4209/aaqr.2017.12.0583, 2018.
903 Jiang, Y., Gao, Z., He, J., Wu, J., and Christakos, G.: Application and Analysis of XCO2 Data from OCO Satellite Using a Synthetic
904 DINEOF–BME Spatiotemporal Interpolation Framework, Remote Sens., 14, 4422, https://doi.org/10.3390/rs14174422, 2022.
905 Kampa, M. and Castanas, E.: Human health effects of air pollution, Environ. Pollut., 151, 362–367,
906 https://doi.org/10.1016/j.envpol.2007.06.012, 2008.
907 Kang, Y., Choi, H., Im, J., Park, S., Shin, M., Song, C.-K., and Kim, S.: Estimation of surface-level NO2 and O3 concentrations
908 using TROPOMI data and machine learning over East Asia, Environ. Pollut., 288, 117711,
909 https://doi.org/10.1016/j.envpol.2021.117711, 2021.
910 Kim, J., Jeong, U., Ahn, M.-H., Kim, J. H., Park, R. J., Lee, H., Song, C. H., Choi, Y.-S., Lee, K.-H., Yoo, J.-M., Jeong, M.-J.,
911 Park, S. K., Lee, K.-M., Song, C.-K., Kim, S.-W., Kim, Y. J., Kim, S.-W., Kim, M., Go, S., Liu, X., Chance, K., Miller, C. C., Al-
912 Saadi, J., Veihelmann, B., Bhartia, P. K., Torres, O., Abad, G. G., Haffner, D. P., Ko, D. H., Lee, S. H., Woo, J.-H., Chong, H.,
913 Park, S. S., Nicks, D., Choi, W. J., Moon, K.-J., Cho, A., Yoon, J., Kim, S., Hong, H., Lee, K., Lee, H., Lee, S., Choi, M., Veefkind,
914 P., Levelt, P. F., Edwards, D. P., Kang, M., Eo, M., Bak, J., Baek, K., Kwon, H.-A., Yang, J., Park, J., Han, K. M., Kim, B.-R.,
915 Shin, H.-W., Choi, H., Lee, E., Chong, J., Cha, Y., Koo, J.-H., Irie, H., Hayashida, S., Kasai, Y., Kanaya, Y., Liu, C., Lin, J.,
916 Crawford, J. H., Carmichael, G. R., Newchurch, M. J., Lefer, B. L., Herman, J. R., Swap, R. J., Lau, A. K. H., Kurosu, T. P., Jaross,
917 G., Ahlers, B., Dobber, M., McElroy, C. T., and Choi, Y.: New era of air quality monitoring from space: Geostationary environment
918 monitoring spectrometer (GEMS), https://doi.org/10.1175/BAMS-D-18-0013.1, 2020a.

https://doi.org/10.5194/essd-2026-443
Preprint. Discussion started: 24 June 2026

Kim, J., Jeong, U., Ahn, M.-H., Kim, J. H., Park, R. J., Lee, H., Song, C. H., Choi, Y.-S., Lee, K.-H., Yoo, J.-M., Jeong, M.-J., Park, S. K., Lee, K.-M., Song, C.-K., Kim, S.-W., Kim, Y. J., Kim, S.-W., Kim, M., Go, S., Liu, X., Chance, K., Miller, C. C., Al-Saadi, J., Veihelmann, B., Bhartia, P. K., Torres, O., Abad, G. G., Haffner, D. P., Ko, D. H., Lee, S. H., Woo, J.-H., Chong, H., Park, S. S., Nicks, D., Choi, W. J., Moon, K.-J., Cho, A., Yoon, J., Kim, S., Hong, H., Lee, K., Lee, H., Lee, S., Choi, M., Veefkind, P., Levelt, P. F., Edwards, D. P., Kang, M., Eo, M., Bak, J., Baek, K., Kwon, H.-A., Yang, J., Park, J., Han, K. M., Kim, B.-R., Shin, H.-W., Choi, H., Lee, E., Chong, J., Cha, Y., Koo, J.-H., Irie, H., Hayashida, S., Kasai, Y., Kanaya, Y., Liu, C., Lin, J., Crawford, J. H., Carmichael, G. R., Newchurch, M. J., Lefer, B. L., Herman, J. R., Swap, R. J., Lau, A. K. H., Kurosu, T. P., Jaross, G., Ahlers, B., Dobber, M., McElroy, C. T., and Choi, Y.: New Era of Air Quality Monitoring from Space: Geostationary Environment Monitoring Spectrometer (GEMS), https://doi.org/10.1175/BAMS-D-18-0013.1, 2020b.

Krotkov, N. A., McLinden, C. A., Li, C., Lamsal, L. N., Celarier, E. A., Marchenko, S. V., Swartz, W. H., Bucsela, E. J., Joiner, J., Duncan, B. N., Boersma, K. F., Veefkind, J. P., Levelt, P. F., Fioletov, V. E., Dickerson, R. R., He, H., Lu, Z., and Streets, D. G.: Aura OMI observations of regional SO_2 and NO_2 pollution changes from 2005 to 2015, Atmospheric Chemistry and Physics, 16, 4605–4629, https://doi.org/10.5194/acp-16-4605-2016, 2016.

Lamsal, L. N., Martin, R. V., Parrish, D. D., and Krotkov, N. A.: Scaling Relationship for NO_2 Pollution and Urban Population Size: A Satellite Perspective, Environ. Sci. Technol., 47, 7855–7861, https://doi.org/10.1021/es400744g, 2013a.

Lamsal, L. N., Martin, R. V., Parrish, D. D., and Krotkov, N. A.: Scaling Relationship for NO2 Pollution and Urban Population Size: A Satellite Perspective, Environ. Sci. Technol., 47, 7855–7861, https://doi.org/10.1021/es400744g, 2013b.

LeCun, Y. A., Bottou, L., Orr, G. B., and Müller, K.-R.: Efficient BackProp, in: Neural Networks: Tricks of the Trade: Second Edition, edited by: Montavon, G., Orr, G. B., and Müller, K.-R., Springer, Berlin, Heidelberg, 9–48, https://doi.org/10.1007/978-3-642-35289-8_3, 2012.

Levelt, P. F., Hilsenrath, E., Leppelmeier, G. W., van den Oord, G. H. J., Bhartia, P. K., Tamminen, J., de Haan, J. F., and Veefkind, J. P.: Science objectives of the ozone monitoring instrument, IEEE Transactions on Geoscience and Remote Sensing, 44, 1199–1208, https://doi.org/10.1109/TGRS.2006.872336, 2006a.

Levelt, P. F., van den Oord, G. H. J., Dobber, M. R., Malkki, A., Visser, H., Vries, J. de, Stammes, P., Lundell, J. O. V., and Saari, H.: The ozone monitoring instrument, IEEE Transactions on Geoscience and Remote Sensing, 44, 1093–1101, https://doi.org/10.1109/TGRS.2006.872333, 2006b.

Li, L. and Wu, J.: Spatiotemporal estimation of satellite-borne and ground-level NO2 using full residual deep networks, Remote Sensing of Environment, 254, 112257, https://doi.org/10.1016/j.rse.2020.112257, 2021.

Li, T., Wu, J., and Wang, T.: Generating daily high-resolution and full-coverage XCO2 across China from 2015 to 2020 based on OCO-2 and CAMS data, Science of The Total Environment, 893, 164921, https://doi.org/10.1016/j.scitotenv.2023.164921, 2023.

Li, T., Wu, J., Wang, Y., and Su, Y.: Improved seamless mapping of surface O3 concentrations using an integrated deep learning framework, Npj Clim. Atmos. Sci., 8, 124, https://doi.org/10.1038/s41612-025-01007-x, 2025.

Liu, G., Shih, K. J., Wang, T.-C., Reda, F. A., Sapra, K., Yu, Z., Tao, A., and Catanzaro, B.: Partial convolution based padding, https://doi.org/10.48550/arXiv.1811.11718, 28 November 2018.

Liu, S., Valks, P., Pinardi, G., De Smedt, I., Yu, H., Beirle, S., and Richter, A.: An improved total and tropospheric NO_2 column retrieval for GOME-2, Atmospheric Measurement Techniques, 12, 1029–1057, https://doi.org/10.5194/amt-12-1029-2019, 2019.

Liu, S., Valks, P., Pinardi, G., Xu, J., Chan, K. L., Argyrouli, A., Lutz, R., Beirle, S., Khorsandi, E., Baier, F., Huijnen, V., Bais, A., Donner, S., Dörner, S., Gratsea, M., Hendrick, F., Karagkiozidis, D., Lange, K., Piters, A. J. M., Remmers, J., Richter, A., Van Roozendael, M., Wagner, T., Wenig, M., and Loyola, D. G.: An improved TROPOMI tropospheric NO_2 research product over Europe, Atmospheric Measurement Techniques, 14, 7297–7327, https://doi.org/10.5194/amt-14-7297-2021, 2021a.

https://doi.org/10.5194/essd-2026-443
Preprint. Discussion started: 24 June 2026

959 Liu, S., Valks, P., Beirle, S., and Loyola, D. G.: Nitrogen dioxide decline and rebound observed by GOME-2 and TROPOMI
960 during COVID-19 pandemic, Air Qual Atmos Health, 14, 1737–1755, https://doi.org/10.1007/s11869-021-01046-2, 2021b.
961 Liu, X., Ran, L., Lin, W., Xu, X., Ma, Z., Dong, F., He, D., Zhou, L., Shi, Q., and Wang, Y.: Measurement report: Variations in
962 surface SO_2 and NO_x mixing ratios from 2004 to 2016 at a background site in the North China Plain, Atmospheric Chemistry and
963 Physics, 22, 7071–7085, https://doi.org/10.5194/acp-22-7071-2022, 2022.
964 Liu, Y., Zhao, J., Song, K., Cheng, C., Li, S., and Cai, K.: Spatiotempo ral evolution analysis of NO2 column density before and
965 after COVID-19 pandemic in henan province based on SI-APSTE model, Sci Rep, 11, 18614, https://doi.org/10.1038/s41598-021-
966 97745-y, 2021c.
967 Loyola, D.: Applications of neural network methods to the processing of earth observation satellite data, Neural Networks, 19,
968 168–177, https://doi.org/10.1016/j.neunet.2006.01.010, 2006.
969 Loyola, D., Gimeno García, S., Lutz, R., Argyrouli, A., Romahn, F., Spurr, R. J. D., Pedergnana, M., Doicu, A., Molina García,
970 V., and Schüssler, O.: The operational cloud retrieval algorithms from TROPOMI on board Sentinel-5 Precursor, Atmospheric
971 Measurement Techniques, 11, 409–427, https://doi.org/10.5194/amt-11-409-2018, 2018.
972 Ma, Y., Liu, T., Yu, Z., Jiang, C., Xu, G., and Lu, Z.: All-weather precipitable water vapor map reconstruction using data fusion
973 and machine learning-based spatial downscaling, Atmos. Res., 296, 107068, https://doi.org/10.1016/j.atmosres.2023.107068, 2023.
974 MacFerrin, M., Amante, C., Carignan, K., Love, M., and Lim, E.: The Earth Topography 2022 (ETOPO 2022) global DEM dataset,
975 Earth System Science Data, 17, 1835–1849, https://doi.org/10.5194/essd-17-1835-2025, 2025.
976 Meng, X., Chen, L., Cai, J., Zou, B., Wu, C.-F., Fu, Q., Zhang, Y., Liu, Y., and Kan, H.: A land use regression model for estimating
977 the NO2 concentration in shanghai, China, Environ. Res., 137, 308–315, https://doi.org/10.1016/j.envres.2015.01.003, 2015.
978 Mentel, T. F., Bleilebens, D., and Wahner, A.: A study of nighttime nitrogen oxide oxidation in a large reaction chamber—the fate
979 of NO2, N2O5, HNO3, and O3 at different humidities, Atmospheric Environment, 30, 4007–4020, https://doi.org/10.1016/1352-
980 2310(96)00117-3, 1996.
981 Mols, A., Boersma, K. F., Denier van der Gon, H., and Krol, M.: An improved bayesian inversion to estimate daily NO_x emissions
982 of paris from TROPOMI NO_2 observations between 2018–2023, Atmospheric Chemistry and Physics, 26, 1497–1513,
983 https://doi.org/10.5194/acp-26-1497-2026, 2026.
984 Monks, P. S., Granier, C., Fuzzi, S., Stohl, A., Williams, M. L., Akimoto, H., Amann, M., Baklanov, A., Baltensperger, U., Bey,
985 I., Blake, N., Blake, R. S., Carslaw, K., Cooper, O. R., Dentener, F., Fowler, D., Fragkou, E., Frost, G. J., Generoso, S., Ginoux,
986 P., Grewe, V., Guenther, A., Hansson, H. C., Henne, S., Hjorth, J., Hofzumahaus, A., Huntrieser, H., Isaksen, I. S. A., Jenkin, M.
987 E., Kaiser, J., Kanakidou, M., Klimont, Z., Kulmala, M., Laj, P., Lawrence, M. G., Lee, J. D., Liousse, C., Maione, M., McFiggans,
988 G., Metzger, A., Mieville, A., Moussiopoulos, N., Orlando, J. J., O'Dowd, C. D., Palmer, P. I., Parrish, D. D., Petzold, A., Platt,
989 U., Pöschl, U., Prévôt, A. S. H., Reeves, C. E., Reimann, S., Rudich, Y., Sellegri, K., Steinbrecher, R., Simpson, D., Ten Brink,
990 H., Theloke, J., Van Der Werf, G. R., Vautard, R., Vestreng, V., Vlachokostas, Ch., and Von Glasow, R.: Atmospheric composition
991 change – global and regional air quality, Atmos. Environ., 43, 5268–5350, https://doi.org/10.1016/j.atmosenv.2009.08.021, 2009.
992 Munro, R., Lang, R., Klaes, D., Poli, G., Retscher, C., Lindstrot, R., Huckle, R., Lacan, A., Grzegorski, M., Holdak, A.,
993 Kokhanovsky, A., Livschitz, J., and Eisinger, M.: The GOME-2 instrument on the Metop series of satellites: instrument design,
994 calibration, and level 1 data processing – an overview, Atmospheric Measurement Techniques, 9, 1279–1301,
995 https://doi.org/10.5194/amt-9-1279-2016, 2016.
996 NOAA National Centers for Environmental Information: ETOPO 2022 15 arc-second global relief model,
997 https://doi.org/10.25921/FD45-GT74, 2022.

https://doi.org/10.5194/essd-2026-443
Preprint. Discussion started: 24 June 2026

998 Noguchi, K., Richter, A., Rozanov, V., Rozanov, A., Burrows, J. P., Irie, H., and Kita, K.: Effect of surface BRDF of various land
999 cover types on geostationary observations of tropospheric NO_2, Atmospheric Measurement Techniques, 7, 3497–3508,
1000 https://doi.org/10.5194/amt-7-3497-2014, 2014.
1001 Palma, L., Peraza, A., Civantos-Prieto, D., Duarte, A., Materia, S., Muñoz, Á. G., Peña-Izquierdo, J., Romero, L., Soret, A., and
1002 Donat, M. G.: Data-driven seasonal climate predictions via variational inference and transformers, npj Clim Atmos Sci, 9, 48,
1003 https://doi.org/10.1038/s41612-026-01320-z, 2026.
1004 Park, T., Liu, M.-Y., Wang, T.-C., and Zhu, J.-Y.: Semantic image synthesis with spatially-adaptive normalization, in: 2019
1005 IEEE/CVF Conference on Computer Vision and Pattern Recognition (CVPR), 2019 IEEE/CVF Conference on Computer Vision
1006 and Pattern Recognition (CVPR), 2332–2341, https://doi.org/10.1109/CVPR.2019.00244, 2019.
1007 Peng, Z., Zhang, B., Wang, D., Niu, X., Sun, J., Xu, H., Cao, J., and Shen, Z.: Application of machine learning in atmospheric
1008 pollution research: A state-of-art review, Science of The Total Environment, 910, 168588,
1009 https://doi.org/10.1016/j.scitotenv.2023.168588, 2024.
1010 Pinardi, G., Lambert, J. C., Granville, J., Van Roozendael, M., Delcloo, A., De Backer, H., Valks, P., and Hao, N.: Overview of
1011 the validation of GOME-2 total and tropospheric NO2 columns, in: EUMETSAT meteorological satellite conference, 2010.
1012 Purchase, M. L., Bending, G. D., and Mushinski, R. M.: Spatiotemporal Variations of Soil Reactive Nitrogen Oxide Fluxes across
1013 the Anthropogenic Landscape, Environ. Sci. Technol., 57, 16348–16360, https://doi.org/10.1021/acs.est.3c05849, 2023.
1014 Qin, K., Rao, L., Xu, J., Bai, Y., Zou, J., Hao, N., Li, S., and Yu, C.: Estimating Ground Level NO2 Concentrations over Central-
1015 Eastern China Using a Satellite-Based Geographically and Temporally Weighted Regression Model, Remote Sens., 9, 950,
1016 https://doi.org/10.3390/rs9090950, 2017.
1017 Qin, K., Gao, H., Liu, X., He, Q., Tiwari, P., and Cohen, J. B.: The global daily High Spatial–Temporal Coverage Merged
1018 tropospheric NO_2 dataset (HSTCM-NO_2) from 2007 to 2022 based on OMI and GOME-2, Earth Syst. Sci. Data, 16, 5287–5310,
1019 https://doi.org/10.5194/essd-16-5287-2024, 2024.
1020 Qu, Y., Wei, J., Xing, H., Shi, X., Ao, Z., and Meng, X.: Global Estimates of Daily Gapless Atmospheric XCH_4 Concentrations
1021 From Satellite and Reanalysis Data During 2003–2020, IEEE Trans. Geosci. Remote Sens., 63, 1–12,
1022 https://doi.org/10.1109/TGRS.2025.3593486, 2025.
1023 Rao, L., Xu, J., Efremenko, D. S., Loyola, D. G., and Doicu, A.: Aerosol Parameters Retrieval From TROPOMI/S5P Using
1024 Physics-Based Neural Networks, IEEE Journal of Selected Topics in Applied Earth Observations and Remote Sensing, 15, 6473–
1025 6484, https://doi.org/10.1109/JSTARS.2022.3196843, 2022.
1026 Ravindra, K., Mor, S., Ameena, Kamyotra, J. S., and Kaushik, C. P.: Variation in Spatial Pattern of Criteria Air Pollutants Before
1027 and During Initial Rain of Monsoon, Environ Monit Assess, 87, 145–153, https://doi.org/10.1023/A:1024650215970, 2003.
1028 Reda, I. and Andreas, A.: Solar position algorithm for solar radiation applications, Solar Energy, 76, 577–589,
1029 https://doi.org/10.1016/j.solener.2003.12.003, 2004.
1030 Richter, A., Burrows, J. P., Nüß, H., Granier, C., and Niemeier, U.: Increase in tropospheric nitrogen dioxide over China observed
1031 from space, Nature, 437, 129–132, https://doi.org/10.1038/nature04092, 2005.
1032 Ronneberger, O., Fischer, P., and Brox, T.: U-net: Convolutional networks for biomedical image segmentation,
1033 https://doi.org/10.48550/arXiv.1505.04597, 18 May 2015.
1034 Russell, A. R., Valin, L. C., and Cohen, R. C.: Trends in OMI NO_2 observations over the united states: Effects of emission control
1035 technology and the economic recession, Atmospheric Chemistry and Physics, 12, 12197–12209, https://doi.org/10.5194/acp-12-
1036 12197-2012, 2012.

https://doi.org/10.5194/essd-2026-443
Preprint. Discussion started: 24 June 2026

1037 Safieddine, S., Clerbaux, C., George, M., Hadji-Lazaro, J., Hurtmans, D., Coheur, P.-F., Wespes, C., Loyola, D., Valks, P., and
1038 Hao, N.: Tropospheric ozone and nitrogen dioxide measurements in urban and rural regions as seen by IASI and GOME-2, Journal
1039 of Geophysical Research: Atmospheres, 118, 10,555-10,566, https://doi.org/10.1002/jgrd.50669, 2013.
1040 Samoli, E., Aga, E., Touloumi, G., Nisiotis, K., Forsberg, B., Lefranc, A., Pekkanen, J., Wojtyniak, B., Schindler, C., Niciu, E.,
1041 Brunstein, R., Dodič Fikfak, M., Schwartz, J., and Katsouyanni, K.: Short-term effects of nitrogen dioxide on mortality: an analysis
1042 within the APHEA project, Eur. Respir. J., 27, 1129–1138, https://doi.org/10.1183/09031936.06.00143905, 2006.
1043 Scheibenreif, L., Mommert, M., and Borth, D.: Toward Global Estimation of Ground-Level NO_2 Pollution With Deep Learning
1044 and Remote Sensing, IEEE Trans. Geosci. Remote Sens., 60, 1–14, https://doi.org/10.1109/TGRS.2022.3160827, 2022.
1045 Sfica, L., Beck, C., Nita, A.-I., Voiculescu, M., Birsan, M.-V., and Philipp, A.: Cloud cover changes driven by atmospheric
1046 circulation in europe during the last decades, International Journal of Meteorology, 41, 221–2230, 2021.
1047 Shao, Y., Zhao, W., Liu, R., Yang, J., Liu, M., Fang, W., Hu, L., Adams, M., Bi, J., and Ma, Z.: Estimation of daily NO2 with
1048 explainable machine learning model in China, 2007–2020, Atmos. Environ., 314, 120111,
1049 https://doi.org/10.1016/j.atmosenv.2023.120111, 2023.
1050 She, L., Zhang, H. K., Li, Z., de Leeuw, G., and Huang, B.: Himawari-8 aerosol optical depth (AOD) retrieval using a deep neural
1051 network trained using AERONET observations, Remote Sensing, 12, 4125, https://doi.org/10.3390/rs12244125, 2020.
1052 She, L., Li, Z., De Leeuw, G., Wang, W., Wang, Y., Yang, L., Feng, Z., Yang, C., and Shi, Y.: Time series retrieval of multi-
1053 wavelength aerosol optical depth by adapting transformer (TMAT) using himawari-8 AHI data, Remote Sensing of Environment,
1054 305, 114115, https://doi.org/10.1016/j.rse.2024.114115, 2024.
1055 Song, W., Jia, H., Li, Z., Tang, D., and Wang, C.: Detecting urban land-use configuration effects on NO2 and NO variations using
1056 geographically weighted land use regression, Atmospheric Environment, 197, 166–176,
1057 https://doi.org/10.1016/j.atmosenv.2018.10.031, 2019.
1058 Stull, R. B.: An introduction to boundary layer meteorology, Springer Science & Business Media, 2012.
1059 Sun, Y., Zeng, Q., Geng, B., Lin, X., Sude, B., and Chen, L.: Deep Learning Architecture for Estimating Hourly Ground-Level
1060 $PM_{2.5}$ Using Satellite Remote Sensing, IEEE Geosci. Remote Sens. Lett., 16, 1343–1347,
1061 https://doi.org/10.1109/LGRS.2019.2900270, 2019.
1062 Sun, Y., Niu, T., He, J., Ma, Z., Liu, P., Xiao, D., Hu, J., Yang, J., and Yan, X.: Classification of circulation patterns during the
1063 formation and dissipation of continuous pollution weather over the sichuan basin, China, Atmospheric Environment, 223, 117244,
1064 https://doi.org/10.1016/j.atmosenv.2019.117244, 2020.
1065 Valks, P., Pinardi, G., Richter, A., Lambert, J.-C., Hao, N., Loyola, D., Van Roozendael, M., and Emmadi, S.: Operational total
1066 and tropospheric NO_2 column retrieval for GOME-2, Atmospheric Measurement Techniques, 4, 1491–1514,
1067 https://doi.org/10.5194/amt-4-1491-2011, 2011.
1068 Veefkind, J. P., Aben, I., McMullan, K., Förster, H., de Vries, J., Otter, G., Claas, J., Eskes, H. J., de Haan, J. F., Kleipool, Q., van
1069 Weele, M., Hasekamp, O., Hoogeveen, R., Landgraf, J., Snel, R., Tol, P., Ingmann, P., Voors, R., Kruizinga, B., Vink, R., Visser,
1070 H., and Levelt, P. F.: TROPOMI on the ESA sentinel-5 precursor: A GMES mission for global observations of the atmospheric
1071 composition for climate, air quality and ozone layer applications, Remote Sensing of Environment, 120, 70–83,
1072 https://doi.org/10.1016/j.rse.2011.09.027, 2012a.
1073 Veefkind, J. P., Aben, I., McMullan, K., Förster, H., de Vries, J., Otter, G., Claas, J., Eskes, H. J., de Haan, J. F., Kleipool, Q., van
1074 Weele, M., Hasekamp, O., Hoogeveen, R., Landgraf, J., Snel, R., Tol, P., Ingmann, P., Voors, R., Kruizinga, B., Vink, R., Visser,
1075 H., and Levelt, P. F.: TROPOMI on the ESA Sentinel-5 Precursor: A GMES mission for global observations of the atmospheric

https://doi.org/10.5194/essd-2026-443
Preprint. Discussion started: 24 June 2026

composition for climate, air quality and ozone layer applications, Remote Sensing of Environment, 120, 70–83, https://doi.org/10.1016/j.rse.2011.09.027, 2012b.

Verhoelst, T., Compernolle, S., Pinardi, G., Lambert, J.-C., Eskes, H. J., Eichmann, K.-U., Fjæraa, A. M., Granville, J., Niemeijer, S., Cede, A., Tiefengraber, M., Hendrick, F., Pazmiño, A., Bais, A., Bazureau, A., Boersma, K. F., Bognar, K., Dehn, A., Donner, S., Elokhov, A., Gebetsberger, M., Goutail, F., Grutter de la Mora, M., Gruzdev, A., Gratsea, M., Hansen, G. H., Irie, H., Jepsen, N., Kanaya, Y., Karagkiozidis, D., Kivi, R., Kreher, K., Levelt, P. F., Liu, C., Müller, M., Navarro Comas, M., Piters, A. J. M., Pommereau, J.-P., Portafaix, T., Prados-Roman, C., Puentedura, O., Querel, R., Remmers, J., Richter, A., Rimmer, J., Rivera Cárdenas, C., Saavedra de Miguel, L., Sinyakov, V. P., Stremme, W., Strong, K., Van Roozendael, M., Veefkind, J. P., Wagner, T., Wittrock, F., Yela González, M., and Zehner, C.: Ground-based validation of the Copernicus Sentinel-5P TROPOMI NO_2 measurements with the NDACC ZSL-DOAS, MAX-DOAS and Pandonia global networks, Atmospheric Measurement Techniques, 14, 481–510, https://doi.org/10.5194/amt-14-481-2021, 2021.

Wang, J.: Global daily 1 km gapless XCO_2 (2003−2023) derived from multi-satellite observations and a spatiotemporal deep learning framework, Environ. Impact Assess. Rev., 117, 108146, https://doi.org/10.1016/j.eiar.2025.108146, 2026.

Wang, J., Li, J., Ye, J., Zhao, J., Wu, Y., Hu, J., Liu, D., Nie, D., Shen, F., and Huang, X.: Fast sulfate formation from oxidation of SO2 by NO2 and HONO observed in beijing haze, Nature Communications, 11, 2844, 2020.

Wang, M., Duan, Y., Zhang, Z., Yuan, Q., Li, X., Han, S., Huo, J., Chen, J., Lin, Y., Fu, Q., Wang, T., Cao, J., and Lee, S.: Reduction in vehicular emissions attributable to the Covid-19 lockdown in Shanghai: insights from 5 years of monitoring-based machine learning, Atmos. Chem. Phys., 23, 10313–10324, https://doi.org/10.5194/acp-23-10313-2023, 2023.

Wang, Y., Yuan, Q., Li, T., Zhu, L., and Zhang, L.: Estimating daily full-coverage near surface O3, CO, and NO2 concentrations at a high spatial resolution over China based on S5P-TROPOMI and GEOS-FP, Isprs J. Photogramm. Remote Sens., 175, 311–325, https://doi.org/10.1016/j.isprsjprs.2021.03.018, 2021.

van Weele, M. and Duynkerke, P. G.: Effect of clouds on the photodissociation of NO2: Observations and modelling, Journal of atmospheric chemistry, 16, 231–255, https://doi.org/10.1007/BF00696898, 1993.

Wei, J., Li, Z., Lyapustin, A., Sun, L., Peng, Y., Xue, W., Su, T., and Cribb, M.: Reconstructing 1-km-resolution high-quality PM2.5 data records from 2000 to 2018 in China: spatiotemporal variations and policy implications, Remote Sensing of Environment, 252, 112136, https://doi.org/10.1016/j.rse.2020.112136, 2021.

Wei, J., Liu, S., Li, Z., Liu, C., Qin, K., Liu, X., Pinker, R. T., Dickerson, R. R., Lin, J., Boersma, K. F., Sun, L., Li, R., Xue, W., Cui, Y., Zhang, C., and Wang, J.: Ground-level NO2 surveillance from space across China for high resolution using interpretable spatiotemporally weighted artificial intelligence, Environ. Sci. Technol., 56, 9988–9998, https://doi.org/10.1021/acs.est.2c03834, 2022.

Wei, W., Bao, Z., Su, Y., Wang, P., and Bai, S.: Research of rapid retrieving models for GOSAT XCO2 based on machine learning, Comput. Geosci., 29, 35, https://doi.org/10.1007/s10596-025-10376-4, 2025.

Xing, J., Baek, B. H., Li, S., Wang, C.-T., Song, G., Ma, S., Zheng, S., Liu, C., Tong, D., Woo, J.-H., Liu, T.-Y., and Fu, J. S.: A Physically Constrained Deep-Learning Fusion Method for Estimating Surface NO_2 Concentration from Satellite and Ground Monitors, Environ. Sci. Technol., 58, 21218–21228, https://doi.org/10.1021/acs.est.4c07341, 2024.

Xu, J., Schüssler, O., Rodriguez, D. G. L., Romahn, F., and Doicu, A.: A Novel Ozone Profile Shape Retrieval Using Full-Physics Inverse Learning Machine (FP-ILM), IEEE Journal of Selected Topics in Applied Earth Observations and Remote Sensing, 10, 5442–5457, https://doi.org/10.1109/JSTARS.2017.2740168, 2017.

https://doi.org/10.5194/essd-2026-443
Preprint. Discussion started: 24 June 2026

Xu, W. Y., Zhao, C. S., Ran, L., Deng, Z. Z., Liu, P. F., Ma, N., Lin, W. L., Xu, X. B., Yan, P., He, X., Yu, J., Liang, W. D., and Chen, L. L.: Characteristics of pollutants and their correlation to meteorological conditions at a suburban site in the North China Plain, Atmospheric Chemistry and Physics, 11, 4353–4369, https://doi.org/10.5194/acp-11-4353-2011, 2011.

Yu, M. and Liu, Q.: Deep learning-based downscaling of tropospheric nitrogen dioxide using ground-level and satellite observations, Science of The Total Environment, 773, 145145, https://doi.org/10.1016/j.scitotenv.2021.145145, 2021.

Yuan, L., Han, W., Meng, J., Wang, Y., Yu, H., and Li, W.: Uncovering the impact of urban functional zones on air quality in China, Atmospheric Chemistry and Physics, 25, 10421–10442, https://doi.org/10.5194/acp-25-10421-2025, 2025.

Zammit-Mangion, A., Cressie, N., and Shumack, C.: On Statistical Approaches to Generate Level 3 Products from Satellite Remote Sensing Retrievals, Remote Sens., 10, 155, https://doi.org/10.3390/rs10010155, 2018.

Zhang, M., Li, S., Xing, J., Song, G., Li, S., Dong, J., Zheng, S., Han, G., and Yang, J.: Enhancing spatiotemporal coverage of satellite-derived high-resolution NO2 data with a super-resolution model, Remote Sens. Environ., 328, 114897, https://doi.org/10.1016/j.rse.2025.114897, 2025a.

Zhang, Q., Boersma, K. F., van der Laan, C., Mols, A., Zhao, B., Li, S., and Pan, Y.: Estimating the variability in NO_x emissions from wuhan with TROPOMI NO_2 data during 2018 to 2023, Atmospheric Chemistry and Physics, 25, 3313–3326, https://doi.org/10.5194/acp-25-3313-2025, 2025b.

Zhang, X. and Gao, J.: Measuring Feature Importance of Convolutional Neural Networks, IEEE Access, 8, 196062–196074, https://doi.org/10.1109/ACCESS.2020.3034625, 2020.

Zhou, Y., Brunner, D., Boersma, K. F., Dirksen, R., and Wang, P.: An improved tropospheric NO_2 retrieval for OMI observations in the vicinity of mountainous terrain, Atmospheric Measurement Techniques, 2, 401–416, https://doi.org/10.5194/amt-2-401-2009, 2009.

Zoogman, P., Liu, X., Suleiman, R. M., Pennington, W. F., Flittner, D. E., Al-Saadi, J. A., Hilton, B. B., Nicks, D. K., Newchurch, M. J., Carr, J. L., Janz, S. J., Andraschko, M. R., Arola, A., Baker, B. D., Canova, B. P., Chan Miller, C., Cohen, R. C., Davis, J. E., Dussault, M. E., Edwards, D. P., Fishman, J., Ghulam, A., González Abad, G., Grutter, M., Herman, J. R., Houck, J., Jacob, D. J., Joiner, J., Kerridge, B. J., Kim, J., Krotkov, N. A., Lamsal, L., Li, C., Lindfors, A., Martin, R. V., McElroy, C. T., McLinden, C., Natraj, V., Neil, D. O., Nowlan, C. R., O'Sullivan, E. J., Palmer, P. I., Pierce, R. B., Pippin, M. R., Saiz-Lopez, A., Spurr, R. J. D., Szykman, J. J., Torres, O., Veefkind, J. P., Veihelmann, B., Wang, H., Wang, J., and Chance, K.: Tropospheric emissions: Monitoring of pollution (TEMPO), Journal of Quantitative Spectroscopy and Radiative Transfer, 186, 17–39, https://doi.org/10.1016/j.jqsrt.2016.05.008, 2017.